Clustered Star Formation in the Center of NGC 253 Contributes to Driving the Ionized Nuclear Wind

E. A. C. Mills[1] , M. Gorski[2] , K. L. Emig[3,4,15] , A. D. Bolatto[5,6] , R. C. Levy[7] , A. K. Leroy[8] , A. Ginsburg[9] ,
J. D. Henshaw[10] , L. K. Zschaechner[11] , S. Veilleux[5] , K. Tanaka[12] , D. S. Meier[13,14] , F. Walter[10] , N. Krieger[10] , and
J. Ott[14]

[1] Department of Physics and Astronomy, University of Kansas, 1251 Wescoe Hall Dr., Lawrence, KS 66045, USA; eacmills@ku.edu
[2] Department of Space, Earth and Environment, Astronomy and Plasma Physics, Chalmers University of Technology, SE-412 96, Gothenburg, Sweden
[3] Leiden Observatory, Leiden University, P.O.Box 9513, NL-2300 RA, Leiden, The Netherlands
[4] National Radio Astronomy Observatory, 520 Edgemont Rd., Charlottesville, VA 22903
[5] Department of Astronomy and Joint Space-Science Institute, University of Maryland, College Park, MD 20742, USA
[6] Visiting Scholar, Flatiron Institute, Center for Computational Astrophysics, New York, NY 10010, USA
[7] Department of Astronomy, University of Maryland, College Park, MD 20742, USA
[8] Department of Astronomy, The Ohio State University, 140 West 18th Avenue, Columbus, OH 43210, USA
[9] Department of Astronomy, University of Florida, 211 Bryant Space Sciences Center, Gainesville, 32611 FL, USA
[10] Max-Planck-Institut für Astronomie, Königstuhl 17, D-69117, Heidelberg, Germany
[11] University of Helsinki, Physicum, Helsingin Yliopisto, Gustaf Hällströin katu 2, 00560 Helsinki, Finland
[12] Department of Physics, Faculty of Science and Technology, Keio University, 3-14-1 Hiyoshi, Yokohama, Kanagawa 223-8522 Japan
[13] New Mexico Institute of Mining & Technology, 801 Leroy Place, Socorro, NM 87801, USA
[14] National Radio Astronomy Observatory, PO Box O, 1003 Lopezville Road, Socorro, NM 87801, USA

Abstract

We present new 3 mm observations of the ionized gas toward the nuclear starburst in the nearby ($D \sim 3.5$ Mpc) galaxy NGC 253. With ALMA, we detect emission from the H40α and He40α lines in the central 200 pc of this galaxy on spatial scales of $\sim$4 pc. The recombination line emission primarily originates from a population of approximately a dozen embedded super star clusters in the early stages of formation. We find that emission from these clusters is characterized by electron temperatures ranging from 7000 to 10,000 K and measures an average singly ionized helium abundance $\langle Y^+ \rangle = 0.25 \pm 0.06$, both of which are consistent with values measured for H II regions in the center of the Milky Way. We also report the discovery of unusually broad line width recombination line emission originating from seven of the embedded clusters. We suggest that these clusters contribute to the launching of the large-scale hot wind observed to emanate from the central starburst. Finally, we use the measured recombination line fluxes to improve the characterization of overall embedded cluster properties, including the distribution of cluster masses and the fractional contribution of the clustered star formation to the total starburst, which we estimate is at least 50%.

Unified Astronomy Thesaurus concepts: Interstellar medium (847); H II regions (694); Young star clusters (1833)

1. Introduction

The barred spiral galaxy NGC 253 (distance: 3.5 Mpc; Rekola et al. 2005) is one of the nearest examples of a galaxy undergoing a nuclear starburst. Apart from this key difference, the stellar component of the nucleus of NGC 253 is in many ways an analog to the Milky Way's center. Both are dominated by a bar potential and have a nearly identical stellar mass within the central 200 pc ($\sim 10^9 \, M_\odot$; Wynn-Williams et al. 1979; Launhardt et al. 2002; Sormani et al. 2020). Additionally, while a supermassive black hole has not been definitively detected in NGC 253 (and no active galactic nucleus (AGN) is present; Müller-Sánchez et al. 2010), the virial mass in the central 20 pc is consistent with the mass of the Milky Way's central black hole ($(4-5) \times 10^6 \, M_\odot$; Rodríguez-Rico et al. 2006; Ghez et al. 2008). However, the star formation environments in the two nuclei are starkly different: within the central half kiloparsec of NGC 253, stars are forming at a rate of 2.8 $M_\odot$ yr^{-1} (Ott et al. 2005; Bendo et al. 2015), fueled by a cold molecular gas reservoir with a mass of $(2-4) \times 10^8 \, M_\odot$ (Mauersberger et al. 1996; Sakamoto et al. 2011; Leroy et al. 2015; Krieger et al. 2019). Compared to the center of the Milky Way, the center of NGC 253 has roughly an

order of magnitude more molecular gas (Dahmen et al. 1998) and a 30–40 times higher star formation rate (Longmore et al. 2013; Barnes et al. 2017).

A significant fraction of the starburst activity in the central 200 pc of NGC 253 is concentrated in a population of embedded young massive clusters. Leroy et al. (2018, hereafter L18) detect 14 compact sources with continuum emission at both 33 and 350 GHz, only one of which is visible at infrared wavelengths (Watson et al. 1996; Kornei & McCrady 2009). The large luminosities of these sources (from which stellar masses of 10^4–$10^6 \, M_\odot$ are inferred), as well as the associated large gas masses of $\sim 5 \times 10^3 \, M_\odot$ to $5 \times 10^5 \, M_\odot$, indicate that these sources are all in the process of forming super star clusters, which are typically defined as having initial stellar masses $>10^5 \, M_\odot$ (Turner et al. 2000; Mengel et al. 2002; Clark et al. 2005). L18 further estimate that at least 20% of the ionizing photons associated with the starburst come from the star formation in these clusters. They also suggest that star formation taking place in these and other undetected lower-mass embedded clusters could account for the entire starburst. Overall, the starburst in NGC 253 is relatively young. Infrared spectra of the unobscured stellar population are consistent with ages of <8 Myr (Kornei & McCrady 2009; Davidge 2016). The deeply obscured cluster population is likely younger:

---

[15] Jansky Fellow of the National Radio Astronomy Observatory.

ALMA observations by L18 require that they must be $\lesssim 5$–10 Myr. They further argue that the theoretical timescale for the formation of clusters still embedded in their natal gas suggests that the embedded clusters should be as young as ~ 1 Myr and consistent with a zero-age main-sequence (ZAMS) stellar population.

While the gas depletion timescale for the starburst nucleus of NGC 253 due to star formation alone is ~ 100 Myr, the nucleus of NGC 253 also drives a massive molecular outflow detected with CO ($M \sim 10^7\ M_\odot$; Bolatto et al. 2013; Zschaechner et al. 2018; Krieger et al. 2019), which is estimated to be additionally depleting the central reservoir at a rate of 10–40 $M_\odot\ \mathrm{yr}^{-1}$. Together with the star formation, this then suggests a gas depletion timescale of only ~ 13–30 Myr. The outflow from NGC 253 is multiphase in nature (Veilleux et al. 2020) and is also detected in dense gas tracers like HCN $1-0$ (Walter et al. 2017), as well as $H_2\ v = 1 - 0$ S(1) (Sugai et al. 2003), Hα (Sharp & Bland-Hawthorn 2010; Westmoquette et al. 2011), and diffuse X-ray emission (Pietsch et al. 2000; Strickland et al. 2002; Bauer et al. 2007), with an extent from 100 pc to more than 1 kpc above the disk and deprojected speeds up to a few hundred kilometers per second. However, the launching points of the outflow are not well localized beyond having an origin in the central 200 pc (Bolatto et al. 2013), where it is believed to be driven purely by the starburst and not to be associated with AGN activity.

As mentioned, although overall the nucleus of NGC 253 is gas-rich, there is no clear candidate for an AGN. A bright nonthermal radio source (Turner & Ho 1985; Ulvestad & Antonucci 1997) has been suggested to be an embedded low-luminosity AGN; however, it does not have the hard X-ray counterpart that would be expected in this case (Müller-Sánchez et al. 2010), and so it may instead be a supernova remnant. The location of a central supermassive black hole and true dynamical center of NGC 253 is thus uncertain; measurements of stellar kinematics suggest a location to within ± 15 pc, a region that includes the nonthermal radio source and an H_2O kilomaser (Henkel et al. 2004; Gorski et al. 2019), several hard X-ray sources (Müller-Sánchez et al. 2010), and a source recently suggested to be the first extragalactic recombination line maser (Báez-Rubio et al. 2018), while low-resolution H92α observations suggest an entirely different kinematic center (Anantharamaiah & Goss 1996).

Altogether, the nucleus of NGC 253 is a complex environment made more difficult to interpret by its nearly edge-on orientation. Both embedded star formation and supernovae are seen in close (projected) proximity. Accurate determinations of the ionizing properties of the cluster stars from the continuum emission then require disentangling the contributions from all of these potential sources. Despite these difficulties, the proximity of NGC 253 makes it the best laboratory for characterizing the dominant mode of star formation in nuclear starbursts.

In this paper, we present new, high-resolution (~ 4 pc) ALMA observations of the 3 mm continuum and the H40α line, both of which trace the ionized gas in the central few hundred parsecs of NGC 253. We use these data to reassess the cluster properties and their relation to the multiphase outflow. We also evaluate the recent claim that NGC 253 hosts the first detected extragalactic recombination line maser source (Báez-Rubio et al. 2018).

2. Observations

2.1. ALMA data

The data used in this analysis were observed using the Atacama Large Millimeter/submillimeter Array (ALMA) in Cycle 5 (Project code 2017.1.00895.S; PI: E.A.C. Mills) in 15 sessions with an average of 45 antennas between 2017 November 25 and December 6. Observations were made in a single frequency setting at 3 mm (ALMA Band 3) toward a single pointing toward the nucleus of NGC 253 with a field of view (half-power beamwidth) of $\sim 1'$ (~ 1 kpc) in three extended configurations (C43-6, C43-7, and C43-8, with baselines ranging from 15 to 8500 m).

The frequency coverage of the data was chosen to match the first of two frequency settings observed at lower resolution ($\sim 2''$, or ~ 35 pc) in Cycle 0 with a 16-antenna array (Project code 2011.0.00172.S; PI: A. Bolatto) and subsequently published in Bolatto et al. (2013), Leroy et al. (2015), and Meier et al. (2015). Four 1.875 GHz wide subbands were centered on frequencies of 86.63, 88.48, 98.52, and 100.38 GHz. The spectral resolution of these data is 0.977 MHz (2.8–3.4 km s^{-1}). This paper focuses on emission from just two lines, the H40α line at 99.022952 GHz and the He40α line at 99.063305 GHz.

The calibration of the data was performed in the Common Astronomy Software Applications package (CASA)[16] using the ALMA pipeline. Imaging of the continuum and the H40α and He40α lines for a single pointing was performed in CASA version 5.4.0 using the tclean task, with a robust weighting of 0.5 to optimize both resolution and sensitivity to the more extended line emission. The final images have beam sizes of $\sim 0''.21 \times 0''.15$ (3.6×2.5 pc) with $0''.03$ pixels and are sensitive to size scales up to $\sim 2''.6$ (~ 44 pc) at 100 GHz, based on ALMA-provided statistics for the typical array configuration of these observations (C43-7). We smoothed both the line and continuum images to a circular beam with a common resolution of $0''.225$ (3.8 pc). The rms noise level for the continuum image is 7 μJy beam^{-1}, while the resulting rms noise level in each ~ 3 km s^{-1} channel for the H40α data was ~ 0.2 mJy beam^{-1} (0.5 K). With almost 13 hr of on-source time on a single field, this is one of the deepest ALMA Band 3 images of any source to date.

We also compare the Band 3 ALMA data to several other ALMA data sets covering the central region of NGC 253. This includes Band 7 images of the HCN $4-3$ line and the 345 GHz continuum (Project code 2015.1.00274.S; PI: A. Bolatto; Leroy et al. 2018), which have a higher native resolution than the Band 3 data ($0''.175$ and $0''.11$ respectively) and so are smoothed to the common resolution of $0''.225$ (3.8 pc). We also include Band 6 continuum images at 240 GHz from the ALMA archive (Project code 2012.1.00789.S; PI: K. Nakanishi). These data have a lower angular resolution of $0''.5 \times 0''.4$, and so for analyses involving comparison with these data we smooth the Band 3 and Band 7 data to match this resolution. Both of these data sets are chosen, as they trace the dense gas and dust surrounding the embedded clusters. The final data set we compare to is archival H26α line data (Project code 2013.1.00735.S; PI: K. Nakanishi; Báez-Rubio et al. 2018). These data also have a somewhat lower angular resolution of

---

[16] https://casa.nrao.edu/

$\sim 0''.3$, and so for analyses including these data we smooth our H40α data to a matching resolution.

2.2. VLA data

The ALMA data are additionally compared to data from the Karl G. Jansky Very Large Array (VLA).[17] The VLA data consist of 22 and 33 GHz continuum emission maps toward the center of NGC 253 (Gorski et al. 2017, 2019). These data have native resolutions that are higher than the ALMA images, with an FWHM beam at 22 (33) GHz of $0''.204 \times 0''.121$ ($0''.096 \times 0''.045$), and are sensitive to emission on spatial scales less than $2''.4$ ($1''.6$). We convolve them to a $0''.225$ beam to match the resolution of the ALMA data for this analysis and regrid them to an identical pixelization. After this convolution the 22 (33) GHz VLA data have a continuum rms noise of 90 (40) μJy beam^{-1}.

We find that the VLA and ALMA reference frames are not exactly aligned. While there is no strong reason to prefer one reference frame over the other, we note that positional errors have been seen in other high-frequency observations made at low elevation with the VLA (Mills et al. 2018) and that these VLA data in particular were taken at a time when the proper refraction calibration was not being applied.[18] We thus apply a slight shift to the VLA data to align them with the positional reference frame of the ALMA images. We perform a cross-correlation between the ALMA continuum image and the VLA images using the task "register_translation" from the Python package scikit-image (van der Walt et al. 2014) and shift the VLA images by $0''.035$ in R.A. and $0''$ in decl. The uncertainty in the alignment from the cross-correlation is $\pm 0''.012$, an order of magnitude smaller than the size scales of the sources studied in this work.

3. Results

The 94 GHz (Band 3) continuum map is shown in the top left panel of Figure 1. This image reveals more than two dozen sources of compact emission, as well as significant extended emission structures, including ridges, diffuse emission, and shells. For comparison, we also show in Figure 1 the map of peak H40α recombination line emission (bottom right) and previously published maps of HCN 4–3 emission (bottom left; L18) and 33 GHz continuum emission (top right; Gorski et al. 2019).

3.1. Identification of Free–Free Emission Sources

We expect that for many locations in the actively star-forming nucleus of NGC 253 there may be a superposition of different types of emission mechanisms (e.g., thermal free–free, non-thermal synchrotron, and thermal dust) associated with different stages of massive star evolution (e.g., supernovae, embedded clusters, and molecular clouds). We use the H40α emission to identify sources of free–free emission corresponding to embedded young clusters, as this line emission originates solely in the ionized gas surrounding these clusters. We note that the presence of H40α does not indicate an absence of nonthermal or dust emission, and the identified clusters may still have

significant nonthermal or dust contributions to their 94 GHz continuum fluxes. We indicate in Figure 1 the location of all of the embedded young clusters identified by L18 (labeled with numbers 1–14); however, we update the position for several of these sources (4, 5, 6, 7, 10, 11, 12, and 14), as they were not well centered on the free–free emission, likely due to physical offsets between the dust continuum and the radio continuum. We take the location of the free–free emission to be more representative of the embedded cluster location. We further identify several additional sources of compact thermal emission that were not identified by L18, which we designate as 7SW, 9NE, 8W, and "10NE" (the last of which was previously identified by Báez-Rubio et al. 2018). While the H40α line emission is strongest from sources 4, 5, 6, 8, 9, 10, 10NE, 11, 12, 13, and 14, recombination line emission is detected toward all of the identified sources, as we discuss in the following sections.

3.1.1. Nonthermal Sources

In addition to the sources labeled in Figure 1, there are a number of strong sources of compact emission visible in the 33 and 94 GHz continuum images, primarily to the south of the main band of identified sources. These sources are most likely dominated by synchrotron emission, as can be seen in a spectral index map ($S_\nu \propto \nu^\alpha$) calculated between the 33 and 94 GHz continuum images (Figure 2). The likely synchrotron-dominated sources exhibit spectral indices $\alpha < -0.5$. Their dominant nonthermal nature is supported by the lack of detectable emission in either HCN 4–3 or H40α. All of these sources are also prominent in 8 and 15 GHz continuum images from Ulvestad & Antonucci (1997), supporting the interpretation that these are nonthermal sources, likely supernova remnants.

3.2. H40α Recombination Line Emission

Spectra of the H40α line toward all sources are extracted from an $r = 0''.18$ (3 pc) aperture and shown in Figure 3. We note that there is a slight overlap in the apertures centered on sources 1, 2, and 3. We attempt to quantify the effects of this overlap by measuring the amount of 3 mm continuum emission present in the overlap region. Sources 1 and 2 have 20%–25% of their total flux in the overlap area, implying that $\sim 10\%$ of the emission in the aperture of each source may be due to contamination from the other source. In contrast, sources 2 and 3 have only 7% of their total flux in the overlap area, implying $< 5\%$ contamination. We thus do not expect these aperture overlaps to affect our results. We conduct Gaussian line fitting for all sources using PySpecKit (Ginsburg & Mirocha 2011). For sources 4, 6, 8, 9NE, 10, 10NE, 11, 12, and 13 we fit two to three separate Gaussian profiles to the H40α line emission to account for the presence of multiple velocity components along the line of sight. The results of the H40α line fits are given in Table 1.

We also conduct Gaussian fits to the HCN 4–3 line profiles extracted from the same aperture, shown in Figure 4. This line traces dense gas associated with the embedded clusters and exhibits many kinematic similarities with the ionized gas traced by H40α. Similar to the H40α fitting, we fit for multiple Gaussian components in sources 4, 6, 7, 7SW, 8, 8W, 9, 9NE, 10, 10NE, 11, 12, and 13. We do not fit for multiple components in sources 1, 2, 3, and 14, as these profiles all exhibit a central dip at the same velocity as the H40α emission. This dip is likely not due to the presence of multiple velocity components, but instead due to HCN self-absorption, which is also seen on
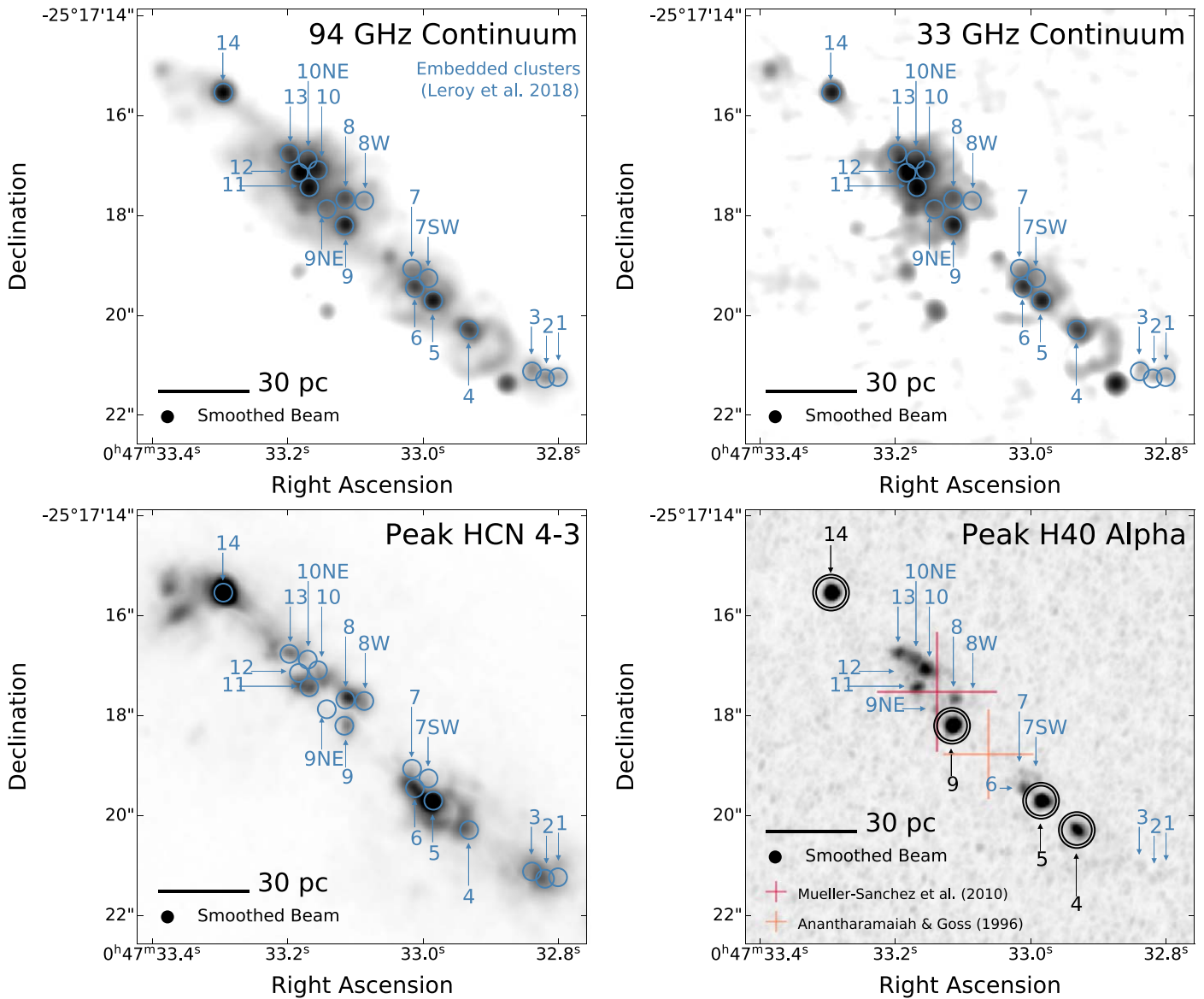
Figure 1. Top left: 94 GHz (3 mm) continuum emission toward the nucleus of NGC 253. Embedded cluster sources from L18 are labeled with numbers 1–14; newly identified sources have additional directional signifiers (e.g., 10NE, as in Báez-Rubio et al. 2018). Circles indicate the 0″.18 (3 pc) radius apertures used to extract recombination line properties. Bottom left: a map of the peak HCN 4−3 emission toward the nucleus of NGC 253 from Leroy et al. (2018). Labels are the same as for top left panel. Top right: 33 GHz continuum emission toward the nucleus of NGC 253 from Gorski et al. (2017). Labels are the same as for the top left panel. Bottom right: a map of the peak H40α emission. Labels are the same as for the top left panel. Circles indicate the larger apertures used to extract continuum properties for four isolated sources (4, 5, 9, and 14) in order to determine representative electron temperatures. The kinematic centers determined by Müller-Sánchez et al. (2010) and Anantharamaiah & Goss (1996) and their 3σ uncertainties are shown as crosses.

comparable spatial scales in lower-excitation lines of multiple species in the embedded cluster Sgr B2[19] in the center of the Milky Way (Mills & Battersby 2017). As a result, these fits do not yield a good estimate of the line widths, and we see large residuals left after fitting. Additionally, we also see some residual absorption at low velocities in sources 5 and 14, which could be a P Cygni profile, indicative of outflowing gas (Levy et al. 2021). Profiles of the HCN 4−3 line overlaid on the H40α line are shown in Figure 5. A comparison of the

kinematics of the H40α and HCN 4−3 lines for each source is given in Table 2.

Measured H40α line widths ($\sigma_{\rm FWHM}$) range from 40 to 100 km s^{-1} for most sources. However, toward sources 4, 6, 10, 10NE, 11, 12, and 13 we measure a much broader line width component ($\Delta v_{\rm FWHM} = 100$–200 km s^{-1}). This component is ~50 km s^{-1} broader than the HCN 4−3 emission located at a comparable velocity centroid. In addition, we detect a broad line width component in sources 10 and 10NE at large positive velocities (270–300 km s^{-1}) that has no HCN counterpart. For both of these components we investigate the possibility of line contamination but find no plausible identification for this feature apart from H40α. Several other sources (5, 7SW, 8, 9NE, and 14) also have H40α emission that is 10–30 km s^{-1} broader than the HCN 4−3 emission. In

---

[19] Sgr B2 is likely the best local analog for the embedded cluster sources we observe in NGC 253. The estimated zero-age main-sequence stellar mass for Sgr B2 (20,000–45,000 $M_\odot$; Schmiedeke et al. 2016; Ginsburg et al. 2018) is comparable to the stellar masses inferred for some of the lowest-mass sources seen here, like the heavily embedded sources 1, 2, and 3, and its line widths are similar (Leroy et al. 2018).
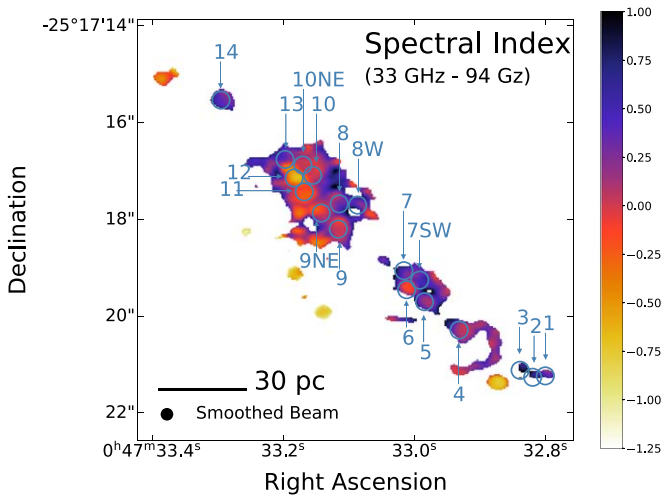
Figure 2. Spectral index map of emission between 33 and 94 GHz. Sources are labeled as in Figure 1. While many sources have a superposition of emission from different mechanisms, sources that are most likely dominated by nonthermal emission have negative spectral indices <-0.5. Sources that are predominately thermal free–free emission are expected to have spectral indices near 0, while sources with spectral indices >0.5 likely have some contribution from dust emission.

contrast, sources 1, 2, 3, and 7 exhibit narrower H40α emission than HCN 4−3 emission. While the HCN line width in sources 1, 2, and 3 is likely underestimated owing to self-absorption, a narrower H40α line profile in source 7 could occur if this is a less evolved source, in which there is a lower stellar mass in the inner region of the central forming cluster compared to the surrounding molecular gas reservoir at larger radii traced by HCN (as discussed in Section 4.3 of Leroy et al. 2018). We discuss the gas kinematics further, including possible origins for the broad line width ionized gas component, in Section 4.

3.2.1. He40α Emission and Ionized Helium Fraction

For several sources we also detect a weaker emission feature corresponding to the He40α line, which is offset by -122.2 km s^{-1} from the H40α line. We do not, however, detect any carbon recombination line emission (the C40α line is offset by -150 km s^{-1} from H40α) toward any source. For sources 5, 9, and 14, we have a clear detection of the He40α line, which can be seen in Figure 3. These three sources are the strongest H40α emitters, and an unambiguous identification of He40α is possible owing to the simple (single-component) structure of their velocity profiles. There are also several sources that have an excess of low-velocity emission that could be due to He40α, but a clear identification is not possible. In sources 4, 8, and 13, a possible He40α feature overlaps with a lower-velocity gas component seen in HCN 4−3, and in source 11 the broad, multicomponent nature of the velocity profile, together with a lack of HCN 4–3 data for this velocity range, makes the identification of He40α emission ambiguous. For the three sources with clear He40α emission, we simultaneously fit two independent Gaussian profiles to both recombination lines, and we report the results of these fits in Table 1.

The simultaneous detection of H40α and He40α emission can be used to determine the helium abundance in these three sources, an indication of enrichment from prior generations of star formation. For the relatively high n states of hydrogen and helium probed by radio/millimeter recombination lines, the level populations should be affected by radiative and collisional
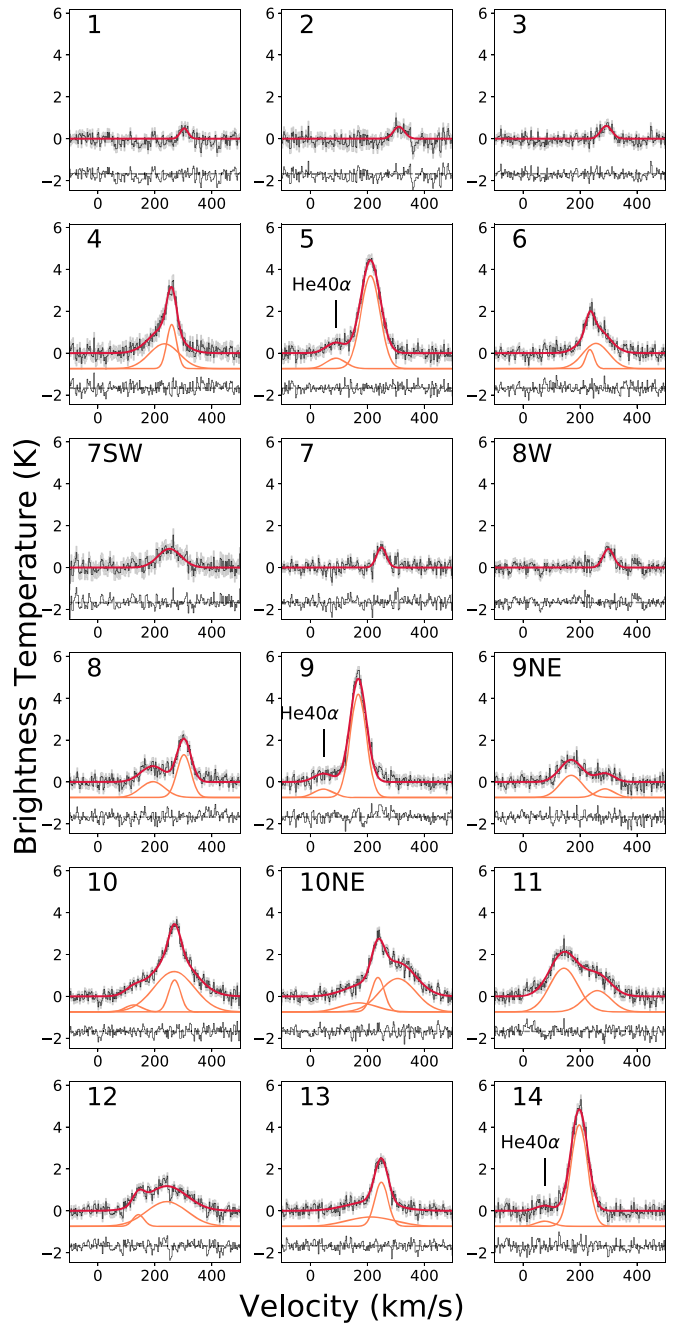
Figure 3. Spectra of H40α toward all sources labeled in Figure 1. One-, two-, and three-component Gaussian fits are conducted to account for gas at different line-of-sight velocities, and the resulting fit for each spectrum is plotted in red. For sources where there are multiple components fit, the individual Gaussian components are also plotted in orange. Residuals from the fitting are plotted below the spectra. The results of these fits are given in Table 1. The location of the He40α line is indicated in the three sources (5, 9, and 14) where it is clearly detected.

effects in the same way. As a result, the ratio of the line areas will then be equal to the ionic abundance ratio (Churchwell et al. 1974; Mezger & Smith 1976). The mass-weighted fraction of singly ionized ^{4}He (Y^+) is then determined as

$$Y^+ = \frac{\int T_B[\text{He}]\,dv\ M_{\text{He}}}{\int T_B[\text{He}]\,dv\ M_{He} + \int T_B[H]\,dv\ M_H}. \quad (1)$$

Table 1
Recombination Line Parameters

| ID	R.A. (deg)	Decl. (deg)	H40α			He40α			Y^+
			v_{cen} (km s^{-1})	σ_{FWHM} (km s^{-1})	Peak T_B (K)	v_{cen} (km s^{-1})	σ_{FWHM} (km s^{-1})	Peak T_B (K)	
1	11.88667	−25.28923	303.1 ± 2.5	32 ± 5	0.5 ± 0.1			<0.18	<0.60
2	11.88675	−25.28924	310.7 ± 3.3	45 ± 7	0.6 ± 0.1			<0.24	<0.62
3	11.88683	−25.28920	292.3 ± 2.2	45 ± 5	0.6 ± 0.1			<0.17	<0.52
4	11.88722	−25.28897	233.5 ± 4.8	123 ± 8	1.2 ± 0.1			<0.16	<0.42
			259.3 ± 1.1	40 ± 3	2.1 ± 0.2				
5	11.88744	−25.28881	210.9 ± 0.5	78 ± 1	4.4 ± 0.1	211.5 ± 0.5	79 ± 12	0.50 ± 0.06	0.31 ± 0.06
6	11.88755	−25.28874	234.7 ± 1.6	34 ± 4	0.9 ± 0.1			<0.18	<0.79
			255.7 ± 2.8	106 ± 5	1.2 ± 0.1				
7SW	11.88747	−25.28868	251.8 ± 3.9	95 ± 9	0.9 ± 0.1			<0.24	<0.52
7	11.88757	−25.28863	249.3 ± 1.2	40 ± 2	1.0 ± 0.1			<0.18	<0.63
8W	11.88786	−25.28825	299.5 ± 1.7	44 ± 3	0.9 ± 0.1			<0.19	<0.45
8	11.88798	−25.28824	193.0 ± 3.6	98 ± 9	0.8 ± 0.0			<0.19	<0.50
			302.3 ± 1.0	57 ± 2	2.0 ± 0.1				
9	11.88798	−25.28839	167.8 ± 0.4	66 ± 0	4.9 ± 0.1	168.3 ± 0.5	79 ± 12	0.40 ± 0.05	0.28 ± 0.05
9NE	11.88809	−25.28830	168.8 ± 2.4	92 ± 6	1.1 ± 0.0			<0.18	<0.41
			287.9 ± 5.6	73 ± 13	0.4 ± 0.1				
10	11.88815	−25.28808	126.1 ± 5.4	68 ± 13	0.3 ± 0.1			<0.14	<0.63
			269.5 ± 1.0	49 ± 3	1.5 ± 0.1				
			267.9 ± 2.0	166 ± 7	1.9 ± 0.1				
10NE	11.88821	−25.28802	169.3 ± 33.6	142 ± 44	0.4 ± 0.1			<0.15	<0.57
			236.8 ± 1.2	53 ± 4	1.6 ± 0.2				
			306.3 ± 9.0	147 ± 11	1.6 ± 0.1				
11	11.88820	−25.28817	143.1 ± 3.6	116 ± 5	2.1 ± 0.1			<0.17	<0.24
			260.8 ± 7.0	110 ± 11	1.0 ± 0.1				
12	11.88826	−25.28809	142.4 ± 2.4	45 ± 7	0.6 ± 0.1			<0.16	<0.53
			242.1 ± 3.6	166 ± 7	1.2 ± 0.0				
13	11.88832	−25.28799	212.1 ± 9.3	193 ± 18	0.4 ± 0.1			<0.18	<0.61
			248.9 ± 0.8	54 ± 2	2.1 ± 0.1				
14	11.88873	−25.28765	197.2 ± 0.5	68 ± 1	4.8 ± 0.1	197.8 ± 0.5	69 ± 22	0.25 ± 0.07	0.17 ± 0.07

Here, $\int T_B[\mathrm{He}]dv$ is the integrated line intensity of the He40α line, M_{He} is the mass of ^{4}He, $\int T_B[\mathrm{H}]dv$ is the integrated line intensity of the H40α line (all integrations are done in the velocity domain), and M_H is the mass of H. The measured Y^+ approaches the mass-weighted abundance of singly ionized helium (Y) if the fraction of doubly ionized helium is negligible (this is generally true for Galactic H II regions; Churchwell et al. 1974) and if the radiation field in these sources is strong enough to fully singly ionize the helium, making the volume-emitting regions of He$^+$ and H$^+$ the same (this should be the case for stars with spectral type O9 and earlier, and it is assumed to be a valid assumption for the clusters here; Churchwell et al. 1974; Mezger et al. 1974). We also look for emission from the He II (64) α line at 98.0795642 GHz, but we do not detect any. Models predict that in the presence of an AGN, recombination lines from He$^+$ would be stronger than the hydrogen recombination lines (Scoville & Murchikova 2013); thus, our nondetection is consistent with other evidence that NGC 253 does not host a central AGN.

We report the derived Y^+ values in Table 1. For sources 5 and 9 we measure Y^+ values ∼0.3, while for source 14 we measure $Y^+ \sim 0.17$. An abundance $Y^+ \sim 0.3$ is consistent with He$^+$/H$^+$ values measured in the same way for H II regions in the Milky Way's center, using lower-frequency (3.6 cm–7 mm) recombination lines. Values in the Milky Way center range from 0.1 to 0.3 in the Arched Filaments and Sgr A West (Mezger & Smith 1976, though these early measurements may have been systematically biased to low values) and up to 0.2–0.45 in the analogous massive protocluster Sgr B2

(de Pree et al. 1996) and 0.39 in the nebula surrounding the luminous blue variable Pistol Star (Lang et al. 1997). As in the Galactic center, the relatively high ratios of He$^+$ to H$^+$ observed in the NGC 253 sources indicate the presence of early O stars and/or Wolf-Rayet stars. Values toward the Milky Way center are also consistent with though somewhat higher than average values in the Milky Way disk ($\langle Y_{disk}^+ \rangle = 0.21 \pm 0.08$; Wenger et al. 2013), which would be expected based on measurements of an increasing helium abundance with decreasing galactocentric radius (Méndez-Delgado et al. 2020). While the lower value seen in source 14 could be an indication of a lower helium abundance in this source, we view it as more likely that this is an underestimate. If the He Strömgren sphere is smaller than both the H Strömgren sphere and the resolution of the observations (as might be expected if the radiation field is not as hard as in other sources), the He40α line will have a larger beam dilution factor, leading to an underestimate of the true helium abundance.

### 3.2.2. Investigating a Proposed Recombination Line Maser in Source 10NE

For source 10NE, we compare the H40α line in our data with archival images of the H26α line at 353.622747 GHz (0″.3 resolution, from project 2013.1.00735.S, PI: K. Naka-nishi). Smoothing the H40α line to a matching 0″.3 resolution and extracting spectra from an $r = 0″.18$ aperture centered on 10NE, we find a consistent flux ratio between the H26α and H40α line of 2.5 ± 0.5, as shown in Figure 6. This corresponds
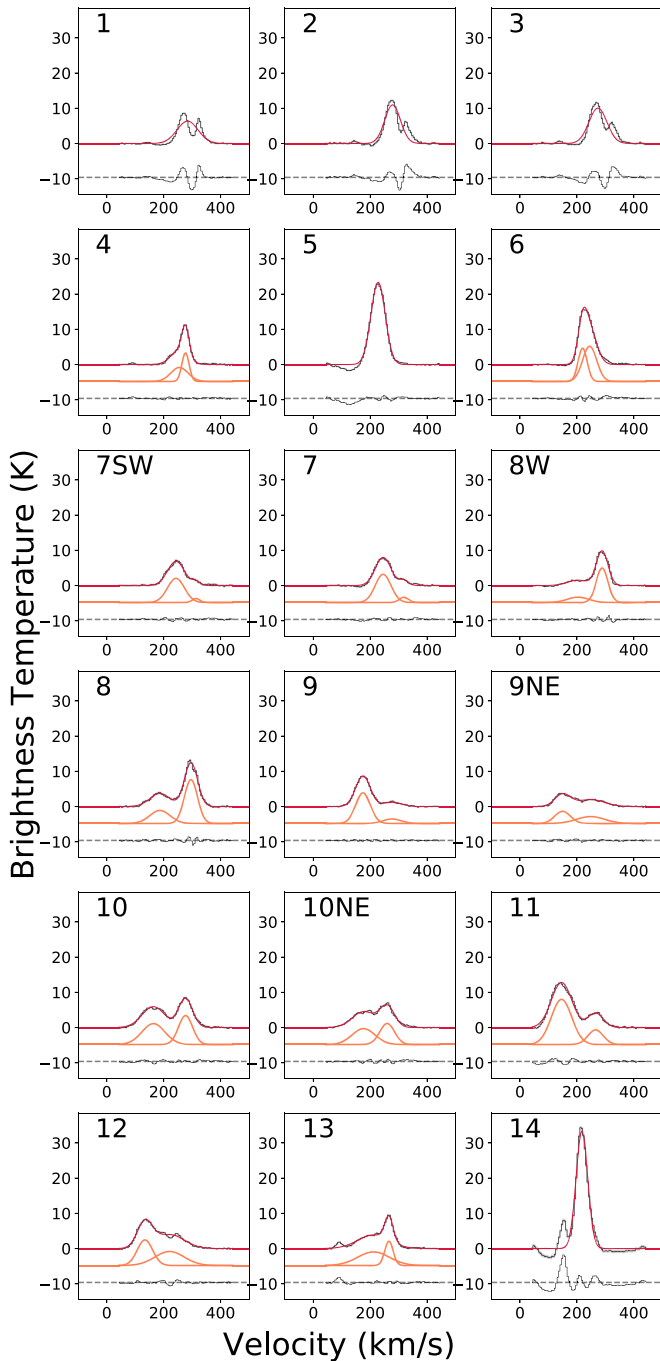
Figure 4. Spectra of HCN 4−3 toward all sources labeled in Figure 1. The velocity axis is chosen to cover the same range as the H40α spectra. One- and two-component Gaussian fits are conducted, and the best-fit model is overplotted in red. Where two Gaussian components are fit, we show the individual components in orange. The residuals of these fits are plotted below the spectra. The results of these fits are given in Table 2.

to a recombination line spectral index $\alpha_L = 0.73 \pm 0.13$. This is slightly smaller than the expectation for simple, optically thin emission ($\alpha_L = 1$) and is consistent with expectations for thermal emission (Prozesky & Smits 2020). It is not consistent with the $\alpha_L > 2.1$ measured between the H26α and H30α line, which was argued to be evidence for stimulated emission in this line (Báez-Rubio et al. 2018). We therefore find no evidence for recombination line maser emission toward this source.
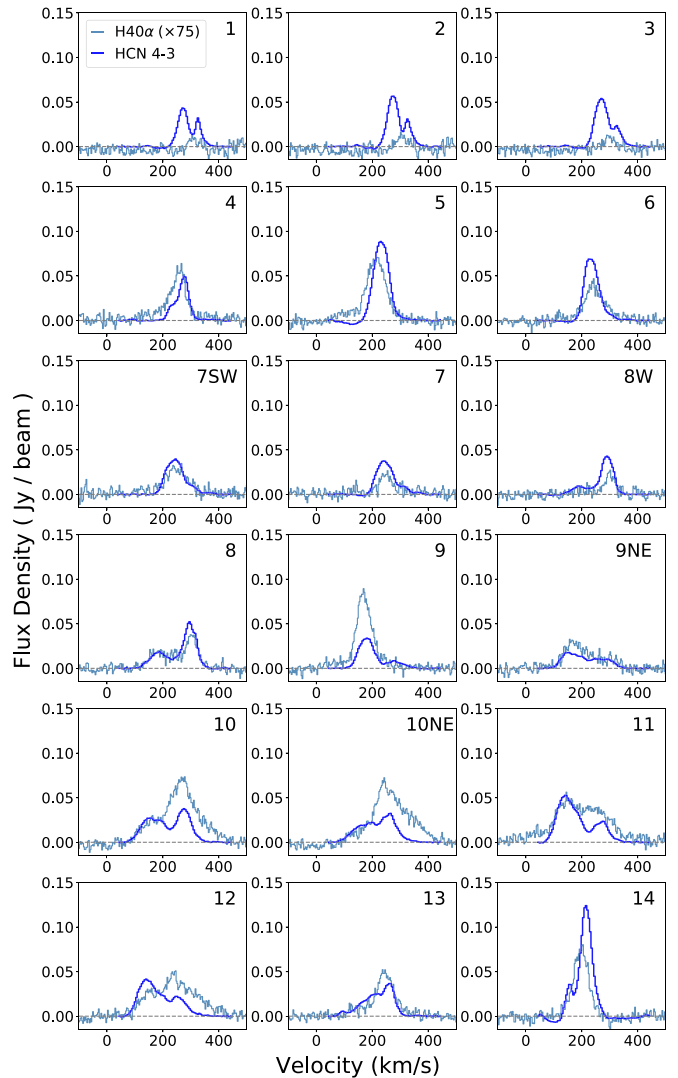
Figure 5. Spectra of H40α (light blue) and HCN 4−3 (dark blue) toward all sources labeled in Figure 1. The H40α spectra are scaled by a factor of 75 in order to facilitate comparison.

3.2.3. The Electron Temperature

In order to infer the total ionizing flux of the detected sources in the nucleus of NGC 253 from the recombination line emission, we must measure a representative electron temperature (T_e). Determining T_e requires a measurement of the free–free flux at the same frequency as the H40α recombination line. A complication is that in many sources the 3 mm continuum also has contributions from both synchrotron and dust emission (see, e.g., Figure 2). To isolate the free–free contribution to the 3 mm continuum flux, we construct five-point spectral energy distributions (SEDs) using our 3 mm (94 GHz) continuum map, 22 GHz and 33 GHz radio maps (Gorski et al. 2017, 2019), our 350 GHz continuum map from L18, and an archival continuum image at 240 GHz (project 2012.1.00789.S, PI: K. Nakanishi). We smooth all of these images to a resolution of $0''.5 \times 0''.4$ in order to match the resolution of the 240 GHz map. Because of the decreased resolution, we select only a representative set of sources (4, 5, 9, and 14) that both are reasonably isolated from surrounding sources and exhibit bright H40α emission. We extract continuum fluxes from $r = 0''.3$ (5.1 pc) apertures centered on these sources and

Table 2
Kinematic Comparison of Ionized and Molecular Gas

| Source | H40α | | HCN (4 − 3) | | Δv_{cen} (H40α - HCN) (km s^{-1}) | Δv_{FWHM} (H40α - HCN) (km s^{-1}) |
	v_{cen} (km s^{-1})	v_{FWHM} (km s^{-1})	v_{cen} (km s^{-1})	v_{FWHM} (km s^{-1})		
1	303.1 ± 2.5	32.3 ± 5.9	283.9 ± 0.2	87.3 ± 0.5	19.2	−55.1
2	310.7 ± 3.3	45.6 ± 7.8	278.5 ± 0.2	65.1 ± 0.5	32.2	−19.5
3	292.3 ± 2.2	45.8 ± 5.2	274.1 ± 0.2	74.5 ± 0.5	18.2	−28.7
4	233.5 ± 4.8	123.3 ± 8.6	255.5 ± 1.2	70.9 ± 1.4	−22.0	52.4
	259.3 ± 1.1	40.5 ± 3.5	276.6 ± 0.2	29.7 ± 0.7	−17.3	10.8
5	210.9 ± 0.5	78.7 ± 1.3	227.5 ± 0.0	59.0 ± 0.1	−16.6	19.7
6	234.7 ± 1.6	34.1 ± 4.8	220.2 ± 0.3	37.2 ± 1.1	14.5	−3.1
	255.7 ± 2.8	106.6 ± 5.2	244.9 ± 1.8	58.1 ± 1.5	10.8	48.6
7SW	251.8 ± 3.9	95.7 ± 9.1	243.2 ± 0.4	70.0 ± 1.0	8.5	25.7
			313.6 ± 1.5	30.5 ± 3.6		
7	249.3 ± 1.2	40.0 ± 2.9	245.1 ± 0.2	65.1 ± 0.6	4.1	−25.1
			318.2 ± 1.0	37.4 ± 2.3		
8W			203.9 ± 0.8	86.5 ± 2.0		
	299.5 ± 1.7	44.3 ± 3.9	288.7 ± 0.1	48.2 ± 0.2	10.8	−3.9
8	193.0 ± 3.6	98.5 ± 9.3	186.9 ± 0.6	83.3 ± 1.4	6.1	15.3
	302.3 ± 1.0	57.9 ± 2.4	295.9 ± 0.1	54.4 ± 0.3	6.3	3.5
9	167.8 ± 0.4	66.8 ± 0.9	174.3 ± 0.1	60.6 ± 0.3	−6.5	6.1
			276.8 ± 0.9	73.9 ± 2.2		
9NE	168.8 ± 2.4	92.7 ± 6.2	149.7 ± 0.5	64.3 ± 1.0	19.1	28.4
	287.9 ± 5.6	73.7 ± 13.6	248.3 ± 1.4	114.9 ± 3.2	39.6	−41.2
10	126.1 ± 5.4	68.5 ± 13.5	163.9 ± 0.4	94.4 ± 1.0	−37.8	−25.9
	267.9 ± 2.0	166.5 ± 7.1				
	269.5 ± 1.0	49.4 ± 3.3	277.0 ± 0.2	58.0 ± 0.5	−7.5	−8.5
10NE	169.3 ± 33.6	142.8 ± 44.1	176.4 ± 0.6	94.0 ± 1.3	−7.1	48.8
	236.8 ± 1.2	53.2 ± 4.0	259.4 ± 0.3	60.8 ± 0.6	−22.6	−7.6
	306.3 ± 9.0	148.0 ± 12.0				
11	143.1 ± 3.6	116.6 ± 5.9	146.1 ± 0.1	84.4 ± 0.4	−2.9	32.2
	260.8 ± 7.0	111.0 ± 11.3	265.8 ± 0.4	62.6 ± 0.9	−5.0	48.4
12	142.4 ± 2.4	46.0 ± 7.7	134.2 ± 0.2	63.6 ± 0.5	8.2	−17.6
	242.1 ± 3.6	166.9 ± 7.9	220.9 ± 1.0	121.2 ± 1.9	21.3	45.7
13	212.1 ± 9.3	193.0 ± 18.6	211.3 ± 0.9	131.4 ± 1.4	0.8	61.7
	248.9 ± 0.8	54.8 ± 2.5	265.6 ± 0.1	34.5 ± 0.5	−16.7	20.3
14	197.2 ± 0.5	68.6 ± 1.1	217.7 ± 0.1	47.9 ± 0.2	−20.4	20.6

subtract the extended continuum background around these sources using an annulus with an inner radius of 0″.3 and an outer radius of 0″.36 (as shown in the bottom right panel of Figure 1). We also smooth our H40α data to match the resolution of the 240 GHz map and extract spectra from a matching $r = 0″.3$ aperture. Fits to these spectra are shown in the left panel of Figure 7.

As seen in the SEDs shown in the right panel of Figure 7, all four of the selected sources have negligible synchrotron contribution, which would appear as a steeply decreasing spectral index ($\alpha \sim -0.75$, where $F \propto \nu^{\alpha}$) at the lowest frequencies. Source 9 further has very little associated dust continuum emission, as a strongly increasing spectral index is not seen at the highest frequencies. We fit the SEDs of all four sources for a range of free–free and dust spectral indices. Given the limited number of constraints available from the five independent frequencies at which we have data, we do not include possible contributions from anomalous microwave emission (AME) in these fits. AME has been observed in extragalactic sources (though not in galaxy nuclei) and peaks at frequencies between 20 and 40 GHz (Hensley et al. 2015). Checking for the presence of AME will require observations of NGC 253 at additional radio frequencies, which would enable more detailed SED fitting of all of the clusters.

To fit the SEDs, we first consider a case in which both the free–free emission and the dust emission are optically thin. For optically thin free–free emission at radio and microwave wavelengths, we expect a power law with a slightly negative spectral index of $\alpha_{ff} = -0.118$ (Draine 2011). This is consistent with the spectral index adopted by Rodríguez-Rico et al. (2006) in their analysis of 7 mm data of NGC 253, though it is slightly shallower than the spectral index adopted by Bendo et al. (2015) in fits to ALMA 3 mm observations on 35 pc scales. Bendo et al. (2015) use a value of $\alpha_{ff} = -0.17$ from Scoville & Murchikova (2013); however, this is more appropriate at submillimeter wavelengths, rather than the predominately longer wavelengths at which we primarily detect free–free emission. For optically thin dust emission at radio and millimeter wavelengths we expect a power law with a spectral index α_d. This spectral index is typically expressed as $2 + \beta$, where β is the dust emissivity coefficient and is expected to be between 1.5 and 2. We fix the spectral index to be 3.8 (with β assumed to be comparable to measurements of $\beta = 1.8$ measured from blackbody fits to ~1 pc resolution observations of the Galactic center embedded cluster Sgr B2; Schmiedeke et al. 2016). Restricting the spectral indices to these values, we fit for the intercepts of both power-law distributions, with the results shown in the right panel of Figure 7. Our fits assuming
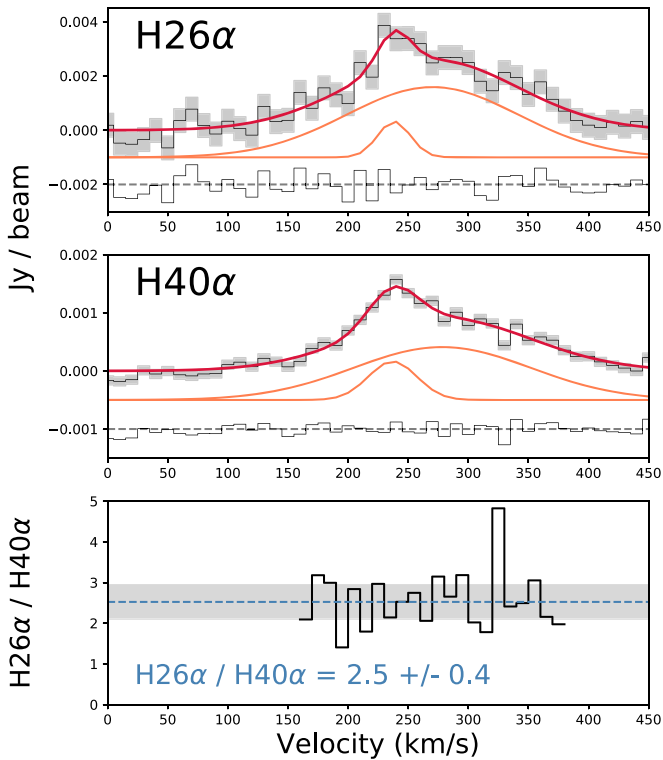
Figure 6. Top and Middle: spectra of H26α and H40α in an $r = 0''.18$ aperture toward source "10NE." Two-component Gaussian fits are conducted for both lines, and the best-fit model is overplotted in red. Individual components of these fits are shown below the spectra in orange. The residuals of these fits are also plotted below the spectra. Bottom: the ratio of the two lines as a function of velocity. The mean value of this ratio is plotted as a light-blue dotted line. We do not see the excess of emission in the H26α line at a velocity around 260 km s^{-1} that was claimed by Báez-Rubio et al. (2018).

optically thin emission result in free–free contributions to the 3 mm flux ranging from 67% to 93% (see Table 3).

We also conduct SED fitting, which allows both spectral indices to vary freely. In this case, both the free–free spectral index and the dust spectral index are allowed to be optically thick. Note that in the optically thick limit the dust spectral index is expected to approach a value of 2. Optically thick free–free emission has a positive, increasing spectral index (up to $\alpha = 2$) at lower frequencies. This is seen in the super star clusters in NGC 5253 (Turner et al. 2000, 1998; Meier et al. 2002), as well as in the Sgr B2 protocluster at the center of the Milky Way, which has a steeply rising spectral index at frequencies up to 22 GHz, turning over near 33 GHz (Protheroe et al. 2008), and for which individual hypercompact H II regions have rising spectral indices up to 60–100 GHz (Zhao & Wright 2011). The best-fit free–free spectral indices range from –0.1 in source 9 (consistent with optically thin free–free emission) to 0.1 in source 14. The best-fit dust spectral indices in sources 4 and 9 could be consistent with optically thin emission, though the spectral index is poorly constrained in source 9. Sources 5 and 14 have spectral indices <3.5, indicating somewhat optically thick dust emission. This is consistent with these clusters being the strongest sources of both 350 GHz dust continuum emission and HCN 4–3 emission (Leroy et al. 2018). The free–free contributions to the 3 mm flux corresponding to fits for these four sources range from 79% to 99%. For comparison, free–free fractions at 100 GHz for the Sgr B2 protocluster from Schmiedeke et al. (2016) range from 0.3

(for the extremely embedded North subcluster) to 0.7 (for the more evolved Main subcluster).

The free-parameter fits to the SEDs of sources 5 and 14 are not consistent with optically thin dust emission. As can be seen in Figure 7, the optically thin fits for these sources underestimate the 94 GHz continuum flux and overestimate the 350 GHz continuum flux. We thus prefer the results of the free-parameter fits for these sources, and for consistency, we adopt the results of the free-parameter fits for all four sources in our remaining analysis. We first use the estimated free–free contributions to the 3 mm continuum flux to derive electron temperatures for sources 4, 5, 9, and 14. To determine the electron temperature T_e, we use the formula derived in Appendix A of Emig et al. (2020), based on Draine (2011) and Gordon & Sorochenko (2002):

$$T_e = 10^4 \text{ K}\left[b_{n+1}\left(\frac{1}{1 + y^+}\right)\left(\frac{R_{\text{LC}}}{31.31 \text{ km s}^{-1}}\right)^{-1} \right.$$
$$\left. \times \left(\frac{\nu}{100 \text{ GHz}}\right)^{1.118} \right]^{0.85}, \qquad (2)$$

where b_{n+1} is the non-LTE departure coefficient, y^+ is the measured abundance ratio of He+ to H+, by number ($N_{\text{He}^+}/N_{\text{H}^+}$), R_{LC} is the ratio of the line-to-continuum emission, and ν is the frequency of the recombination line in GHz.

Parameter b_{n+1} is determined via interpolation from values given in Storey & Hummer (1995). The departure coefficients vary with electron density, and we use coefficients corresponding to densities of $n_e = 10^4$ and 10^5 cm^{-3} to determine a range of T_e values. Our choice of electron densities is primarily based on prior measurements of n_e for H II regions in NGC 253, which find $n_e \geqslant 10^4$ cm^{-3} (Ulvestad & Antonucci 1997; Mohan et al. 2005). In particular, Mohan et al. (2005) found that only 10% of the H40α emission can be modeled with an $n_e = 10^4$ cm^{-3} component and suggested that the presence of higher-density ionized gas is required to fit this emission. This is also consistent with modeling of the radio and millimeter continuum emission toward the Sgr B2 protocluster, which is composed of numerous (ultra)compact HII regions with n_e ranging from 10^4 to 10^6 cm^{-3} (Schmiedeke et al. 2016; Sánchez-Monge et al. 2017).

Parameter y^+ is is related to the mass-weighted abundances Y^+ reported in Table 1 by the equation

$$Y^+ = \frac{y^+ M_{\text{He}}}{y^+ M_{\text{He}} + M_H}. \qquad (3)$$

The ratio of the line-to-continuum emission R_{LC} is given by

$$R_{\text{LC}} = \frac{\int T_L \Delta v}{f_{\text{ff}} T_C}, \qquad (4)$$

where T_C is the brightness temperature of the 3 mm continuum, T_L is the brightness temperature of the recombination line, f_{ff} is the fraction of the 3 mm continuum that comes from free–free emission, and Δv is the FWHM line width of the recombination line in km s^{-1}.

The values of T_e derived from this equation range from 6400 to 11,000 K, with a mean value of $\langle T_e \rangle = 8000$ K. We report these values in Table 3. For comparison, we also report the electron temperatures that would be determined by adopting the free–free fraction from the optically thin SED fits. These are
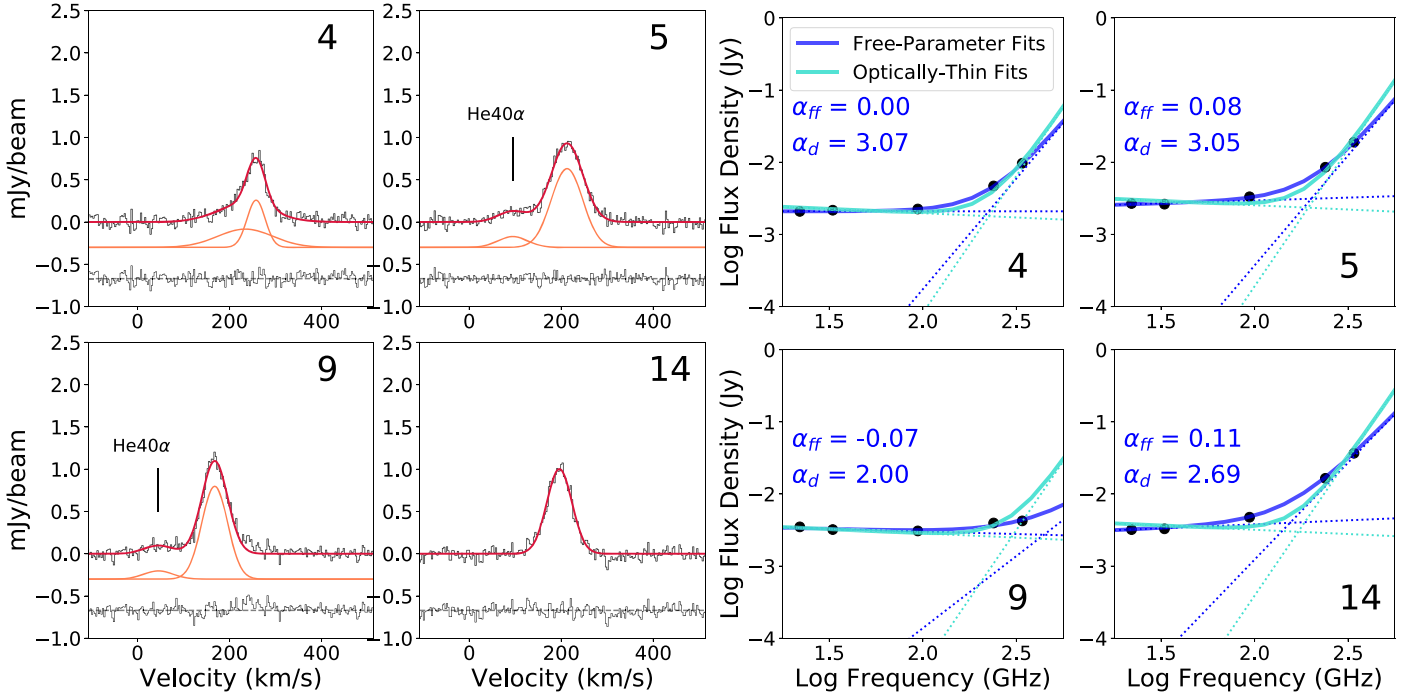
Figure 7. Left: line fits to H40α spectra extracted from the larger (0″.3) apertures used to measure the continuum fluxes for the four isolated sources shown in the second panel of Figure 1. One- and two-component Gaussian fits are conducted, and the best-fit model is overplotted in red. Where two Gaussian components are fit, we show the individual components in orange. The residuals of these fits are plotted below the spectra. Right: fits to the SED composed of continuum measurements at 22, 33, 94, 240, and 350 GHz. Continuum fluxes are extracted from a 0″.3 aperture and background subtracted using an annulus with an inner (outer) radius of 0″.3 (0″.36). The individual contributions of free–free and dust emission are plotted as dotted lines, while the resulting composite is plotted as a solid curve. The cyan lines show fits that fix the spectral indices of the free–free and dust emission to their optically thin values. The dark-blue lines show fits where both spectral indices are allowed to freely vary.

Table 3
Electron Temperatures

Source	4	5	9	14
α_{dust} [a]	3.8	3.8	3.8	3.8
α_{ff} [a]	−0.118	−0.118	−0.118	−0.118
f_{ff}	0.87	0.78	0.93	0.68
T_e [b]	6600 ± 700	6600 ± 700	7400 ± 800	9100 ± 900
α_{dust}	3.1 ± 0.9	3.0 ± 0.5	< 3.7	2.6 ± 0.3
α_{ff}	0.0 ± 0.1	0.1 ± 0.1	-0.1 ± 0.1	0.1 ± 0.1
f_{ff}	0.95	0.89	1.01	0.76
T_e [b]	7100 ± 700	7400 ± 800	7900 ± 800	10000 ± 1000

Notes.
[a] Spectral indices fixed to optically thin values.
[b] T_e ranges determined for $n_e = 10^4$ cm^{-3} and $n_e = 10^5$ cm^{-3}.

slightly lower but are generally consistent given the uncertainties in T_e due to the range of n_e values we adopt for determining the departure coefficient. The electron temperatures we measure are higher than the values measured in NGC 253 using lower-resolution data (3700–4500 K; Bendo et al. 2015). One contributing source of this discrepancy is the higher electron density we have adopted to determine the departure coefficient, as Bendo et al. (2015) assume $n_e = 10^3$ cm^{-3}. The electron temperatures we infer are quite consistent with values measured for H II regions in the Milky Way's central 200 pc (typically 6000–8000 K, with values >10,000 K in individual hypercompact H II regions; Goss et al. 1985; de Pree et al. 1996; Lang et al. 2001). These values are representative of the electron temperature gradient observed in the Milky Way disk, which reaches a minimum at the Galactic center that

corresponds with a maximum in the radial metallicity gradient (Quireza et al. 2006). However, low values are also seen in some other massive star-forming regions in the Milky Way disk (e.g., 8500 K in W51; Ginsburg et al. 2015).

3.2.4. Revised Cluster Ionizing Fluxes

We estimate the flux of Lyman continuum photons (Q_c) in s^{-1} for each embedded cluster using the following expression, which is valid at high frequencies where the free–free continuum opacity $\tau_{\mathrm{ff}} \ll 1$ (Rubin 1968; Condon 1992; Ulvestad & Antonucci 1997):

$$Q_c = 7.5 \times 10^{49} \left(\frac{D}{\mathrm{Mpc}} \right)^2 \left(\frac{T_e}{10^4 \ \mathrm{K}} \right)^{-0.45}$$
$$\times \left(\frac{\nu}{\mathrm{GHz}} \right)^{0.1} \left(\frac{S_{\nu,\mathrm{ff}}}{\mathrm{mJy}} \right). \tag{5}$$

Here ν is the representative continuum frequency in GHz, T_e is the electron temperature (for sources for which we do not have a measurement of T_e, we adopt $\langle T_e \rangle = 8000$ K), D is the distance to the source in Mpc, and $S_{\nu,\mathrm{ff}}$ is the free–free flux at 3 mm. For sources 4, 5, 9, and 14 we have estimates of the fraction of the 3 mm continuum flux that is due to free–free emission from the SED fitting. For the remaining sources we use the adopted $\langle T_e \rangle$ to invert Equation (2) in order to determine a mean line-to-continuum ratio $\langle R_{\mathrm{LC}} \rangle$. For $\langle T_e \rangle = 8000^{+300}_{-1500}$ K (covering the range of temperature variations for the four sources we measure), we derive $\langle R_{\mathrm{LC}} \rangle = 28^{+5}_{-2}$ km s^{-1}. We then apply this ratio to the measured H40α line fluxes to derive the corresponding free–free

Table 4
Stellar Properties of Clusters

ID	$\log_{10} Q_{tot}$ (s^{-1})		$\log_{10} M_*$ ($M_\odot$)		$\log_{10} M_{gas}$ ($M_\odot$)
	H40α	33 GHz[a]	H40α	33 GHz[a]	HCN 4−3[a]
1	$50.6^{+0.2}_{-0.2}$	50.9	$4.0^{+0.2}_{-0.2}$	4.3	4.9
2	$50.8^{+0.2}_{-0.2}$	50.9	$4.2^{+0.2}_{-0.2}$	4.3	4.7
3	$50.8^{+0.2}_{-0.2}$	50.7	$4.2^{+0.2}_{-0.2}$	4.1	5.1
4	$51.7^{+0.1}_{-0.1}$	51.6	$5.1^{+0.1}_{-0.1}$	5.0	5.1
5	$51.9^{+0.1}_{-0.1}$	52.0	$5.3^{+0.0}_{-0.1}$	5.4	5.3
6	$51.6^{+0.2}_{-0.2}$	51.9	$5.0^{+0.2}_{-0.2}$	5.3	3.6
7SW	$51.3^{+0.2}_{-0.2}$		$4.7^{+0.2}_{-0.2}$		
7	$50.9^{+0.2}_{-0.2}$	51.1	$4.3^{+0.3}_{-0.1}$	4.5	4.5
8W	$51.0^{+0.2}_{-0.2}$		$4.4^{+0.2}_{-0.2}$		
8	$51.6^{+0.2}_{-0.2}$	51.4	$5.0^{+0.2}_{-0.1}$	4.8	5.2
9	$51.9^{+0.1}_{-0.1}$	52.1	$5.3^{+0.0}_{-0.1}$	5.5	4.7
9NE	$51.5^{+0.2}_{-0.2}$		$4.9^{+0.2}_{-0.2}$		
10	$51.4^{+0.2}_{-0.2}$	51.9	$4.8^{+0.2}_{-0.2}$	5.3	5.2
10NE	$51.5^{+0.2}_{-0.2}$		$4.9^{+0.2}_{-0.1}$		
11	$51.9^{+0.2}_{-0.2}$	52.2	$5.3^{+0.2}_{-0.2}$	5.6	4.5
12	$51.7^{+0.2}_{-0.2}$	52.6	$5.1^{+0.2}_{-0.2}$	6.0	4.1
13	$51.7^{+0.2}_{-0.2}$	51.4	$5.1^{+0.2}_{-0.2}$	4.8	5.2
14	$51.9^{+0.1}_{-0.1}$	52.1	$5.3^{+0.1}_{-0.0}$	5.5	5.7
Total	52.8	53.1	6.2	6.5	6.2

Note.
[a] Values from Leroy et al. (2018).

flux at 3 mm:

$$S_{\nu,\mathrm{ff}} = \frac{\int S_{\mathrm{H40}\alpha} \Delta v}{\langle R_{\mathrm{LC}} \rangle}. \qquad (6)$$

The resulting Q_c values are presented in Table 4. Typical uncertainties on these values due to the uncertainty in the adopted T_e are 0.1–0.2 dex. We compare these to the L18 estimates of Q_c from the 33 GHz continuum, which assumed that the 33 GHz fluxes are entirely due to free–free emission. For the majority of the detected sources, the ionizing fluxes we infer from the H40α line are consistent with the fluxes determined by L18, within the uncertainties deriving from our temperature measurements. However, there are several sources where the Lyman continuum fluxes we derive are substantially smaller than the L18 values. The largest difference is seen for source 12, for which we estimate a Q_c that is nearly an order of magnitude less than estimated by L18. This source was flagged by L18 as having an abnormally high free–free contribution to the 350 GHz continuum (71%), based on the assumption that the 33 GHz flux is entirely due to free–free emission. Given the relatively small amount of free–free emission at 3 mm that is implied by the H40α fluxes, combined with the negative spectral index seen for this source in Figure 2, our measurements indicate that the 33 GHz continuum for this source has a substantial synchrotron component. The same appears to be true for sources 1, 6, 10, and 11, though to a significantly lesser extent than in source 12. These sources have smaller discrepancies, being lower than the 33 GHz continuum-derived Q_c by 0.3–0.5 dex. Sources 6 and 11 were also noted by L18 as having apparently large free–free contributions to the 350 GHz continuum flux (63% and 41%, respectively). In contrast,

source 10 had only a moderate estimated free–free contribution (11%), and source 1 had one of the lowest estimated free–free contributions to the 350 GHz continuum, only 3%. We further discuss these results and possible sources of uncertainties in both methods of deriving Q_c in Section 4.3.

4. Discussion

Below, we include additional discussion of several of the results from these new ALMA observations, including the detection of broad line width hydrogen recombination line emission from a number of the embedded clusters, and the update of embedded stellar cluster properties compared to the L18 values derived from the radio continuum emission.

4.1. Kinematic Comparison with HCN 4−3

To facilitate comparison between the kinematics of the ionized gas traced by H40α and the dense molecular gas traced by HCN 4−3, we construct a position–velocity (PV) diagram of the central emission along the plane of NGC 253 in both lines (Figure 8). Examining the PV diagram, we see that emission in H40α extends beyond HCN 4−3 for many sources, consistent with our analysis of the spectra, which found that the H40α emission is broader than the HCN 4−3 emission in the majority (12/18) of the sources. We note that the lower-velocity extent of the H40α emission seen in Figure 8 does have a somewhat ambiguous interpretation, as this can include a contribution from He40α (which is offset by -122 km s^{-1}) as was identified in sources 5, 9, and 14. However, this contamination is not present at larger velocities, and we see a clear excess of high-velocity emission toward sources 10, 10NE, and 6. Toward source 10NE in particular, there is a near-complete absence of corresponding HCN emission at velocities $\gtrsim 270$ km s^{-1}. The PV diagram also shows the presence of systematic velocity offsets in sources 4, 5, and 14, where the H40α emission appears to be shifted to lower velocities by ~ 20 km s^{-1} compared to the HCN 4−3 emission. As described in detail in Levy et al. (2021), these three clusters all show signatures of outflows in higher-resolution data of dense molecular tracers, including HCN 4−3.

As mentioned in Section 3.2, we find broad ($\Delta v_{\mathrm{FWHM}} > 100$ km s^{-1}) H40α line emission toward seven of the sources studied here: 4, 6, 10, 10NE, 11, 12, and 13. A complication in interpreting these apparently broad line widths, illustrated in the PV diagram, is that several of these sources are on lines of sight that intersect multiple distinct kinematic components. If these components are not well resolved, these can lead to an apparent broadening of the observed line profiles (Leroy et al. 2015). These kinematic components may be spatially separated, for example, corresponding to the near and far sides of an "x2" family of orbits (Binney et al. 1991; Sormani et al. 2015), analogous to the "twisted ring" or "orbital streams" seen in the Milky Way center (Molinari et al. 2011; Kruijssen et al. 2015; Henshaw et al. 2016). Such nuclear rings, with radii of a few hundred parsecs, are ubiquitously observed at the center of many barred galaxies (e.g., Comerón et al. 2010), and their presence is explained by models of gas flow in barred galaxies (Krumholz & Kruijssen 2015; Torrey et al. 2017; Sormani & Li 2020). In NGC 253, sources 8 and 13 are characteristic of the high-velocity gas, with their strongest emission at velocities of 250–300 km s^{-1}, while sources 5 and 9 are characteristic of the low-velocity gas, with their strongest emission peaking
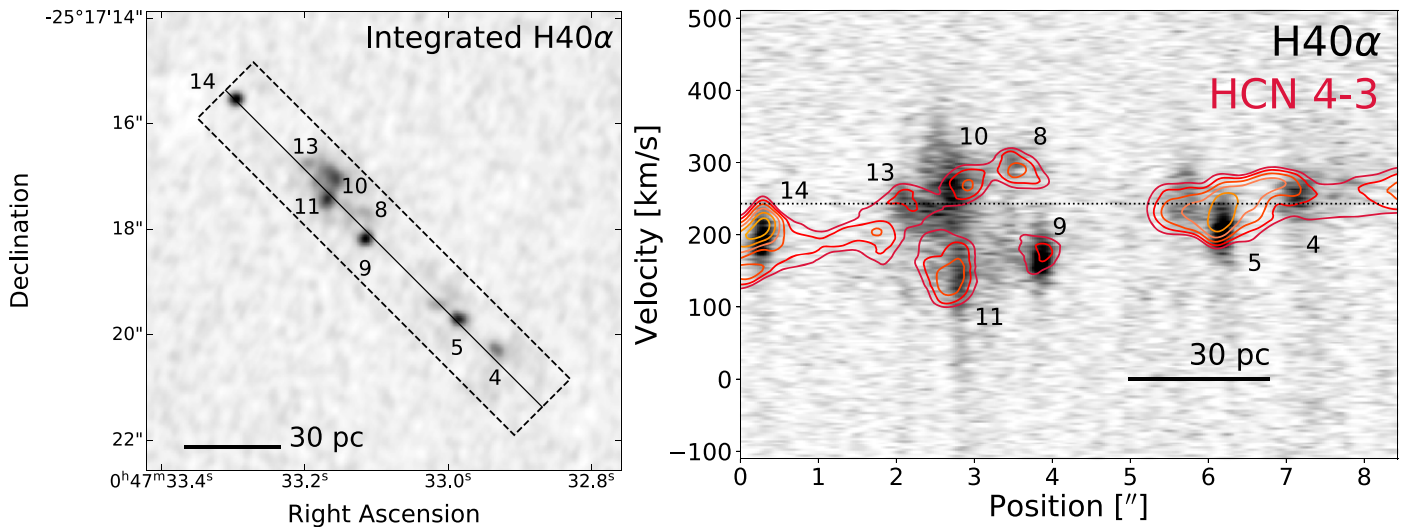
Figure 8. Left: map of integrated Hα emission showing the orientation and width of the slit used to extract a PV diagram. Right: PV diagram of H40α emission (gray scale) compared to HCN 4–3 emission (red contours) along the same slit. The horizontal dotted line shows the rest-frame velocity of NGC 253. Emission at large positive velocities is seen between sources 10 and 13 in H40α but not in HCN 4–3. While there also appears to be large negative-velocity emission extending away from many of the sources (e.g., 4, 5, 9, 11, 13), this is contaminated by the presence of He40α emission.

between $\sim$150 and 200 km s^{-1}. As both velocity components may be present toward many of the embedded clusters, we have made sure to fit complex line profiles with both a low- and high-velocity component, so that this kinematic complexity is not interpreted as an exaggerated line width. We find that the H40α line widths toward these sources, even when fitting multiple components to the line profiles, are significantly broader than observed toward the other clusters (which have $\Delta v_{\mathrm{FWHM}} < 100$ km s^{-1}).

4.2. The Nature of the Broad Line Width H40α Emission

We suggest that the large velocity extent of the H40α line seen in sources 4, 6, 10, 10NE, 11, 12, and 13 is evidence that the embedded clusters in the nuclear starburst of NGC 253 are contributing to driving the hot ionized wind component of the multiphase outflow. The observed widths of the H40α line in these sources ($\Delta v_{\mathrm{FWHM}} \sim 100$–200 km s^{-1}; $\sigma \sim 40$–90 km s^{-1}) are substantially larger than the virial line widths for these clusters ($\sigma \sim 20$ km s^{-1}). The H40α is also $\sim$50 km s^{-1} broader than the HCN 4$-$3 emission at a comparable velocity, implying that the ionized gas is substantially less bound to the cluster than the dense ($\gtrsim 10^3$ cm^{-3}; Kauffmann et al. 2017) molecular gas, which may still be fueling star formation in the clusters. We further detect a broad line width component in sources 10 and 10NE at large positive velocities (270–300 km s^{-1}) that has no clear counterpart in HCN 4$-$3. If the observed broad line widths are tracing the hot wind, this component could correspond to compact emission associated with the northern extension of the inner superwind, which has been previously undetected owing to obscuration from the fore-ground disk of the galaxy (Sharp & Bland-Hawthorn 2010; Westmoquette et al. 2011). This would represent the counter-part to the southern extension seen in X-ray and ionized gas tracers with velocities of 100 ± 50 km s^{-1} (Pietsch et al. 2000; Sharp & Bland-Hawthorn 2010; Westmoquette et al. 2011). While these seven sources represent the clearest examples of broad line width H40α emission, several other sources (5, 7SW, 8, 9NE, and 14) also have H40α emission that is 10–30 km s^{-1} broader than the HCN 4$-$3 emission.

We note that the high-velocity, broad line width emission detected toward sources 10, 10NE, 11, and 12 originates in a $1''.2$ (20 pc) region that overlaps with the apparent kinematic center of NGC 253 (Müller-Sánchez et al. 2010). Some of the large velocity dispersion observed in the H40α line toward these sources could then be due at least in part to the range of orbital velocities expected for sources and/or extended ionized gas lying within 5–10 pc of a supermassive black hole, similar to the velocity spread (± 200 km s^{-1}) seen for molecular gas in the circumnuclear disk of the Milky Way (e.g., Christopher et al. 2005). However, a complication of this interpretation is that the orientation of the velocity gradient of this gas is perpendicular to the geometry of the overall nuclear disk. While this is not impossible, we view it as more likely that a velocity gradient perpendicular to the disk would be associated with an outflow.

If the high-velocity emission in the vicinity of sources 10, 10NE, 11, and 12 were to originate from the central few parsecs, this outflow is unlikely to be driven by the black hole itself, as there is no indication of an active black hole, which would be expected to emit simultaneously at X-ray, radio, and IR wavelengths (Engelbracht et al. 1998; Brunthaler et al. 2009; Fernández-Ontiveros et al. 2009; Müller-Sánchez et al. 2010). A weak AGN is also unlikely to be responsible for ionizing this gas, given that observations of submillimeter recombination lines around the luminous Type II Seyfert NGC 1068 have failed to detect emission (Izumi et al. 2016). The AGN in starburst galaxy NGC 4945 has also been shown not to dominate the ionization of the nuclear region (Marconi et al. 2000; Spoon et al. 2000; Emig et al. 2020). Models further predict that in the presence of an AGN, recombination lines from He^{++} would be stronger than the hydrogen recombination lines (Scoville & Murchikova 2013), and we do not detect any emission from the HeII (64) α line at 98.0795642 GHz.

4.3. Clustered Star Formation in NGC 253

L18 identified a population of 14 compact sources of millimeter dust and spectral line emission toward the nucleus of NGC 253, which they interpreted as embedded clusters, based

on the close association of the dust continuum emission at 350 GHz with radio continuum emission at 33 GHz. Only one of these sources was previously known (source 5) from HST observations, where it was identified as a highly obscured super star cluster (Watson et al. 1996; Kornei & McCrady 2009). Assuming that the 33 GHz continuum is entirely dominated by free–free continuum, L18 estimated the ionizing fluxes of these clusters and their corresponding stellar masses.

Using observations of the H40α recombination line, we have reassessed the properties of the embedded clusters, testing the assumption that the 33 GHz radio continuum is dominated by thermal free–free emission. Using the recombination line fluxes and new measurements of the electron temperature T_e for four of these sources, we have made independent estimates of Q_c for the 14 sources identified by L18, as well as four newly identified sources. We find that sources 1, 6, 10, 11, and 12 all have a lower Lyman continuum flux than estimated by L18. In most cases, this is likely because the 33 GHz continuum contains an additional contribution from synchrotron emission (see Figure 2), as was postulated by L18 for a number of these sources, based on the apparently large amount of free–free flux that would be present at 350 GHz, if the 33 GHz continuum flux were entirely due to free–free emission. However, we also find that an apparently large contribution of free–free emission as extrapolated from the 33 GHz flux to the flux at 350 GHz is not necessarily an indication of substantial synchrotron contamination. Some sources likely do have a significant free–free contribution at 350 GHz, as they do not show negative spectral indices in Figure 2. For example, the SED of source 9 (Figure 7) shows extremely weak dust emission compared to sources 4, 5, and 14, consistent with the estimate by L18 that the free–free contribution at 350 GHz would be 32%. Altogether, we find a slightly lower total ionizing flux contribution from the embedded clusters ($\log[Q_{tot}] = 52.8$) compared to L18, who estimated $\log[Q_{tot}] = 53.1$. That this difference is not larger is due primarily to the contribution from the four sources not cataloged by L18.

We note, however, that significant uncertainties remain in the determination of the Lyman continuum flux. First, all Q_c values, both those derived from 33 GHz and those derived from recombination lines, should be treated as lower limits, as any dust in the H II region will directly absorb some fraction of the Lyman continuum photons, reducing the number of ionizations and leading to an underestimate of Q_c. We also note that while recombination-line-derived Q_c values that are less than those of L18 can be well explained as a result of synchrotron emission, we also find a Q_c for source 13 that is significantly larger than in L18. This is more difficult to explain but could be the result of somewhat optically thick 33 GHz emission, or perhaps a significantly lower electron temperature, though our uncertainties cover a wide range of T_e from ~6000 to 11,000 K. Ultimately, reducing this uncertainty in the T_e measurements for the embedded clusters is essential for future work.

There are two main sources of uncertainty in the T_e measurements. First, the electron temperature depends sensitively on the assumed electron density n_e, which is used to determine the departure coefficients b_n. Parsec-scale observations of additional recombination lines would help with this by allowing us to model the electron density. Subparsec imaging of the thermal gas (from either radio/millimeter continuum or recombination lines) would also be useful to better constrain source sizes, which would give an independent constraint on

the electron densities. Currently, subparsec imaging has only been completed for the dust continuum associated with these clusters (Levy et al. 2021). Second, the measurement of the electron temperatures requires full SED modeling to make a good estimate of the amount of free–free emission contributing to the total continuum emission. Accurately determining the free–free continuum in all of the embedded cluster sources will require parsec-resolution measurements of the continuum emission at additional submillimeter wavelengths. Lacking this, we cannot accurately determine the amount of free–free emission at radio and millimeter wavelengths.

Using our Q_c values, we determine a corresponding stellar mass for the embedded clusters, following the same method as L18 and calculating a mass based on Starburst99 calculations for a ZAMS stellar population (Leitherer et al. 1999). The stellar mass M_* relates to the rate of production of ionizing Lyman continuum photons (Q_c) as

$$M_* \sim \frac{Q_c}{4 \times 10^{46}} M_\odot. \tag{7}$$

The masses we derive are sensitive to the assumption of the age of the stellar population. Cluster masses derived for NGC 4945 (Emig et al. 2020), for which the estimated age of the starburst is 5 Myr, are substantially more massive, as an older stellar population produces fewer ionizing photons per unit mass. Adopting a burst age of 5 Myr for NGC 253 would increase the masses derived here by about an order of magnitude. However, our observations continue to support the adoption of a ZAMS population, as originally argued by L18. Our detection of the He recombination line emission favors a young cluster age, as the H-ionizing radiation from massive stellar populations at high metallicities decreases steeply after ~3 Myr (e.g., Levesque & Leitherer 2013), and the He-ionizing radiation decreases even more steeply (e.g., Levesque et al. 2012). Additionally, we can also make a direct comparison with NGC 4945 to determine a relative age for the two bursts. As seen in Emig et al. (2020), there is substantially more nonthermal emission (due to supernova remnants) intermixed with the cluster emission. The clusters in NGC 4945 also have smaller gas fractions (typically an order of magnitude less than the stellar mass). Together, these differences support the assumption that the cluster ages in NGC 253 are significantly younger.

As expected, the stellar masses of the embedded clusters that we infer from the Q_c values are also generally lower than the masses estimated by L18. Once again, the largest difference is for source 12: the stellar mass we infer for this source is lower by a factor of 8, making it no longer the most massive source. The most massive embedded clusters are now sources 9, 11, and 14 (each with an inferred stellar mass of $2 \times 10^5 M_\odot$). The new sources (7SW, 8W, 9NE, and 10NE) have inferred stellar masses of $(3–8) \times 10^4 M_\odot$. While low, these masses are still larger than found for embedded clusters 1, 2, 3, and 7, which have inferred stellar masses of $(1–2) \times 10^4 M_\odot$.

Overall, we find a minimum total ionizing flux from the clusters of $Q_c = 6.3 \times 10^{52}$ s^{-1}, or 20% of the total ionizing flux of the nuclear starburst as originally estimated by Bendo et al. (2015). However, Bendo et al. (2015) make a number of different assumptions in their calculation of Q_c that make a direct comparison invalid. They assume a slightly smaller distance (2.44 Mpc vs. 2.5 Mpc), a lower electron temperature (3900 K vs. 8000 K) and electron density (10^3 cm^{-3} vs. 10^4 cm^{-3}), and their expression for Q_c includes a frequency

dependence of $\nu^{0.17}$ instead of $\nu^{0.1}$. If the calculation of Q_c in Bendo et al. (2015) via their Equation (3) instead adopted the values from our analysis, then their estimated Q_c would be smaller by a factor of 2.4. We then find that the clusters contribute at least 50% of the total ionizing flux of the starburst. This result confirms the finding of L18 that the embedded massive clusters represent an important mode of the overall starburst, which may even be the dominant mode, depending on the extent to which the Q_c we measure is affected by dust in the embedded clusters, or whether there is a nonzero Lyman continuum escape fraction. This result is also consistent with findings that clustered star formation is a preferred mode in starburst environments in the Milky Way center, where a high cluster formation efficiency ($\sim$40%) is measured in the densest part of the Sgr B2 protocluster (Ginsburg & Kruijssen 2018).

4.4. Evolution of the Starburst

Characterizing the age and evolution of the central starburst in NGC 253 is important both for inferring the current overall stellar content of the clusters and for determining how the evolution of the starburst drives the observed outflows emanating from the nucleus. The candidate protoclusters in the NGC 253 nucleus appear to still be embedded in or associated with their natal molecular clouds. L18 find that 7 out of the 14 embedded clusters they identify have higher gas masses than stellar masses. From our new estimate of the total stellar masses of the embedded clusters, we find that this is comparable to the total gas mass associated with these sources from L18 (Table 4). This suggests that many of these sources are still in the process of forming and supports the assumption of a ZAMS population for the overall NGC 253 starburst, compared to the older burst age of 5 Myr adopted by Emig et al. (2020) for the central starburst in NGC 4945.

However, among the NGC 253 sources there are some indications that a range of evolutionary stages are present. We find that not all of the embedded clusters identified by L18 have ionized gas emission coincident with the dust continuum. In particular, the new positions assigned to sources 4, 10, 11, and 12 based on the location of their H40α emission all have an offset (2–4 pc) from the peaks of nearby dust continuum emission identified by L18. Source 10NE is also significantly offset ($\sim$7 pc) from the dust continuum peaks near sources 10 and 13. These offsets are comparable to or larger than the cluster sizes, which L18 measure to have FWHM diameters of 2.5–4.5 pc. This could indicate that these clusters are less embedded and so are more evolved than sources like 5, 8, 13, and 14 that have nearly coincident dust and free–free emission. However, the visibility of this spatial offset is a function of the orientation of the source with respect to the observer. For example, although there appears to be little offset between ionized and molecular gas in source 5, this is the only embedded cluster that is visible in near-IR HST observations (Watson et al. 1996; Kornei & McCrady 2009). This could indicate that it is one of the least embedded clusters (either because it has cleared most of its natal gas or because it is located on the front side of the molecular cloud), or alternatively it could be the only cluster visible in the near-IR because of a hole in the overall extinction screen toward the center of NGC 253.

The spatial offsets between ionized and molecular gas could also be a sign that the star formation in an individual giant molecular cloud is not entirely contemporaneous and that the clouds may contain clusters or subclusters of slightly different ages. This is seen in the Milky Way center, where at high resolutions the Sgr B2 protocluster breaks up into two separate concentrations offset by a few parsecs, with the northern (N) concentration less evolved than the main (M) concentration: it has less radio continuum emission at lower frequencies and more dust continuum emission at higher frequencies (Schmiedeke et al. 2016). Even earlier stages of star formation are also seen to be distributed throughout the southernmost part of the parent molecular cloud (Ginsburg et al. 2018).

If we assign relative ages to the embedded clusters based on fraction of mass in gas versus stars, the youngest sources would be 1, 2, 3, 8, and 14, which have gas masses from L18 that are 2–9 times larger than stellar masses we infer here (Table 4). For sources 1, 2, and 3 in particular, the stellar masses are more than 100 times smaller than the cluster virial mass. This is very similar to what is seen in Sgr B2, where the estimated stellar mass of the protocluster (20,000–45,000 $M_\odot$; Schmiedeke et al. 2016; Ginsburg et al. 2018) is also $\sim$2 orders of magnitude less than the gas mass of the whole cloud. The oldest sources would be 6, 9, 11, and 12, which all have stellar masses 4–20 times larger than the gas masses. This is consistent with the analysis of Rico-Villas et al. (2020), who find that sources 5, 6, 7, 9, 10, and 12 are more evolved than the embedded clusters 1, 2, 3, 4, 8, 13, and 14.

We have also found that several of the embedded clusters appear to have a significant flux contribution from nonthermal radio emission, particularly sources 6, 11, and 12. This emission is most likely due to synchrotron radiation from compact supernova remnants (Ulvestad & Antonucci 1997). This could result from a chance superposition with older regions of star formation, or it could be an indication that these clusters are sufficiently evolved to have experienced several supernovae. Given that these three candidate protoclusters also have some of the lowest gas masses, we believe it is likely that these sources (as well as source 10NE, which had no counterpart in L18 owing to the lack of corresponding HCN 4−3 emission) represent some of the most evolved clusters associated with the NGC 253 nuclear starburst.

5. Conclusions

We report on new, high-resolution observations of the 3 mm continuum and H40α and He40α line emission toward a population of embedded super star clusters in the central 200 pc of NGC 253. Below, we summarize our main findings.

1. We measure electron temperatures for the ionized gas associated with a subset of four of the embedded clusters (4, 5, 9, and 14) and find that these range from $T_e = 7000$ to 10, 000 K.

2. For three of the embedded clusters (5, 9, and 14) we also measure an average mass-weighted singly ionized helium abundance of $\langle Y^+ \rangle = 0.25 \pm 0.6$. This is comparable to ionized helium abundances observed toward the center of the Milky Way.

3. Using the H40α recombination line fluxes and the derived electron temperatures, we present revised estimates for the ionizing fluxes Q_c of the embedded clusters. From these measurements we infer a slightly lower value for the total stellar mass of the clusters, which we attribute to the contribution of synchrotron emission to the radio continuum previously used to determine these

values. However, based on the increased electron temperatures we measure compared to those in Bendo et al. (2015), we now estimate that at least 50% of the nuclear starburst in NGC 253 originates in a clustered mode of star formation.

4. We identify seven sources that have exceptionally broad line width H40α emission ($\Delta v_{\mathrm{FWHM}} \sim 100$–$200$ km s^{-1}). These line widths are ~ 50 km s^{-1} broader than the molecular gas profiles of these sources measured from HCN $4-3$. We suggest that these embedded clusters contribute to driving the ionized component of the multiphase outflow originating in the nucleus of NGC 253.

ORCID iDs

E. A. C. Mills ⓘ https://orcid.org/0000-0001-8782-1992
M. Gorski ⓘ https://orcid.org/0000-0001-9300-354X
K. L. Emig ⓘ https://orcid.org/0000-0001-6527-6954
A. D. Bolatto ⓘ https://orcid.org/0000-0002-5480-5686
R. C. Levy ⓘ https://orcid.org/0000-0003-2508-2586
A. K. Leroy ⓘ https://orcid.org/0000-0002-2545-1700
A. Ginsburg ⓘ https://orcid.org/0000-0001-6431-9633
J. D. Henshaw ⓘ https://orcid.org/0000-0001-9656-7682
L. K. Zschaechner ⓘ https://orcid.org/0000-0002-9919-8672
S. Veilleux ⓘ https://orcid.org/0000-0002-3158-6820
K. Tanaka ⓘ https://orcid.org/0000-0001-8153-1986
D. S. Meier ⓘ https://orcid.org/0000-0001-9436-9471
F. Walter ⓘ https://orcid.org/0000-0003-4793-7880
N. Krieger ⓘ https://orcid.org/0000-0003-1104-2014
J. Ott ⓘ https://orcid.org/0000-0001-8224-1956

References

Anantharamaiah, K. R., & Goss, W. M. 1996, ApJL, 466, L13
Báez-Rubio, A., Martín-Pintado, J., Rico-Villas, F., & Jiménez-Serra, I. 2018, arXiv:1810.07213
Barnes, A. T., Longmore, S. N., Battersby, C., et al. 2017, MNRAS, 469, 2263
Bauer, M., Pietsch, W., Trinchieri, G., et al. 2007, A&A, 467, 979
Bendo, G. J., Beswick, R. J., D'Cruze, M. J., et al. 2015, MNRAS, 450, L80
Binney, J., Gerhard, O. E., Stark, A. A., Bally, J., & Uchida, K. I. 1991, MNRAS, 252, 210
Bolatto, A. D., Warren, S. R., Leroy, A. K., et al. 2013, Natur, 499, 450
Brunthaler, A., Castangia, P., Tarchi, A., et al. 2009, A&A, 497, 103
Christopher, M. H., Scoville, N. Z., Stolovy, S. R., & Yun, M. S. 2005, ApJ, 622, 346
Churchwell, E., Mezger, P. G., & Huchtmeier, W. 1974, A&A, 32, 283
Clark, J. S., Negueruela, I., Crowther, P. A., & Goodwin, S. P. 2005, A&A, 434, 949
Comerón, S., Knapen, J. H., Beckman, J. E., et al. 2010, MNRAS, 402, 2462
Condon, J. J. 1992, ARA&A, 30, 575
Dahmen, G., Huttemeister, S., Wilson, T. L., & Mauersberger, R. 1998, A&A, 331, 959
Davidge, T. J. 2016, ApJ, 818, 142
de Pree, C. G., Gaume, R. A., Goss, W. M., & Claussen, M. J. 1996, ApJ, 464, 788
Draine, B. T. 2011, Physics of the Interstellar and Intergalactic Medium (Princeton, NJ: Princeton University Press)
Emig, K. L., Bolatto, A. D., Leroy, A. K., et al. 2020, ApJ, 903, 50
Engelbracht, C. W., Rieke, M. J., Rieke, G. H., Kelly, D. M., & Achtermann, J. M. 1998, ApJ, 505, 639
Fernández-Ontiveros, J. A., Prieto, M. A., & Acosta-Pulido, J. A. 2009, MNRAS, 392, L16
Ghez, A. M., Salim, S., Weinberg, N. N., et al. 2008, ApJ, 689, 1044
Ginsburg, A., Bally, J., Barnes, A., et al. 2018, ApJ, 853, 171
Ginsburg, A., Bally, J., Battersby, C., et al. 2015, A&A, 573, A106
Ginsburg, A., & Kruijssen, J. M. D. 2018, ApJL, 864, L17
Ginsburg, A., & Mirocha, J. 2011, PySpecKit: Python Spectroscopic Toolkit, ascl:1109.001
Gordon, M. A., & Sorochenko, R. L. 2002, Radio Recombination Lines. Their Physics and Astronomical Applications, Vol. 282 (Berlin: Springer)
Gorski, M., Ott, J., Rand, R., et al. 2017, ApJ, 842, 124
Gorski, M. D., Ott, J., Rand, R., et al. 2019, MNRAS, 483, 5434
Goss, W. M., Schwarz, U. J., van Gorkom, J. H., & Ekers, R. D. 1985, MNRAS, 215, 69P
Henkel, C., Tarchi, A., Menten, K. M., & Peck, A. B. 2004, A&A, 414, 117
Henshaw, J. D., Longmore, S. N., Kruijssen, J. M. D., et al. 2016, MNRAS, 457, 2675
Hensley, B., Murphy, E., & Staguhn, J. 2015, MNRAS, 449, 809
Izumi, T., Nakanishi, K., Imanishi, M., & Kohno, K. 2016, MNRAS, 459, 3629
Kauffmann, J., Goldsmith, P. F., Melnick, G., et al. 2017, A&A, 605, L5
Kornei, K. A., & McCrady, N. 2009, ApJ, 697, 1180
Krieger, N., Bolatto, A. D., Walter, F., et al. 2019, ApJ, 881, 43
Kruijssen, J. M. D., Dale, J. E., & Longmore, S. N. 2015, MNRAS, 447, 1059
Krumholz, M. R., & Kruijssen, J. M. D. 2015, MNRAS, 453, 739
Lang, C. C., Goss, W. M., & Morris, M. 2001, AJ, 121, 2681
Lang, C. C., Goss, W. M., & Wood, O. S. 1997, ApJ, 474, 275
Launhardt, R., Zylka, R., & Mezger, P. G. 2002, A&A, 384, 112
Leitherer, C., Schaerer, D., Goldader, J. D., et al. 1999, ApJS, 123, 3
Leroy, A. K., Bolatto, A. D., Ostriker, E. C., et al. 2015, ApJ, 801, 25
Leroy, A. K., Bolatto, A. D., Ostriker, E. C., et al. 2018, ApJ, 869, 126
Levesque, E. M., Leitherer, C., Ekstrom, S., Meynet, G., & Schaerer, D. 2012, ApJ, 751, 67
Levesque, E. M., & Leitherer, C. 2013, ApJ, 779, 170
Levy, R. C., Bolatto, A. D., Leroy, A. K., et al. 2021, ApJ, 912, 4
Longmore, S. N., Bally, J., Testi, L., et al. 2013, MNRAS, 429, 987
Marconi, A., Oliva, E., van der Werf, P. P., et al. 2000, A&A, 357, 24
Mauersberger, R., Henkel, C., Wielebinski, R., Wiklind, T., & Reuter, H.-P. 1996, A&A, 305, 421
Meier, D. S., Turner, J. L., & Beck, S. C. 2002, AJ, 124, 877
Meier, D. S., Walter, F., Bolatto, A. D., et al. 2015, ApJ, 801, 63
Méndez-Delgado, J. E., Esteban, C., García-Rojas, J., Arellano-Córdova, K. Z., & Valerdi, M. 2020, MNRAS, 496, 2726
Mengel, S., Lehnert, M. D., Thatte, N., & Genzel, R. 2002, A&A, 383, 137
Mezger, P. G., & Smith, L. F. 1976, A&A, 47, 143
Mezger, P. G., Smith, L. F., & Churchwell, E. 1974, A&A, 32, 269
Mills, E. A. C., & Battersby, C. 2017, ApJ, 835, 76
Mills, E. A. C., Ginsburg, A., Clements, A. R., et al. 2018, ApJL, 869, L14
Mohan, N. R., Goss, W. M., & Anantharamaiah, K. R. 2005, A&A, 432, 1
Molinari, S., Bally, J., Noriega-Crespo, A., et al. 2011, ApJL, 735, L33
Müller-Sánchez, F., González-Martín, O., Fernández-Ontiveros, J. A., Acosta-Pulido, J. A., & Prieto, M. A. 2010, ApJ, 716, 1166
Ott, J., Weiss, A., Henkel, C., & Walter, F. 2005, ApJ, 629, 767
Pietsch, W., Vogler, A., Klein, U., & Zinnecker, H. 2000, A&A, 360, 24
Protheroe, R. J., Ott, J., Ekers, R. D., Jones, D. I., & Crocker, R. M. 2008, MNRAS, 390, 683
Prozesky, A., & Smits, D. P. 2020, MNRAS, 491, 2536
Quireza, C., Rood, R. T., Bania, T. M., Balser, D. S., & Maciel, W. J. 2006, ApJ, 653, 1226
Rekola, R., Richer, M. G., McCall, M. L., et al. 2005, MNRAS, 361, 330
Rico-Villas, F., Martín-Pintado, J., González-Alfonso, E., Martín, S., & Rivilla, V. M. 2020, MNRAS, 491, 4573
Rodríguez-Rico, C. A., Goss, W. M., Zhao, J.-H., Gómez, Y., & Anantharamaiah, K. R. 2006, ApJ, 644, 914
Rubin, R. H. 1968, ApJ, 154, 391
Sakamoto, K., Mao, R.-Q., Matsushita, S., et al. 2011, ApJ, 735, 19

Sánchez-Monge, Á., Schilke, P., Schmiedeke, A., et al. 2017, A&A, 604, A6

Schmiedeke, A., Schilke, P., Möller, T., et al. 2016, A&A, 588, A143

Scoville, N., & Murchikova, L. 2013, ApJ, 779, 75

Sharp, R. G., & Bland-Hawthorn, J. 2010, ApJ, 711, 818

Sormani, M. C., Binney, J., & Magorrian, J. 2015, MNRAS, 449, 2421

Sormani, M. C., & Li, Z. 2020, MNRAS, 494, 6030

Sormani, M. C., Magorrian, J., Nogueras-Lara, F., et al. 2020, MNRAS, 499, 7

Spoon, H. W. W., Koornneef, J., Moorwood, A. F. M., Lutz, D., & Tielens, A. G. G. M. 2000, A&A, 357, 898

Storey, P. J., & Hummer, D. G. 1995, MNRAS, 272, 41

Strickland, D. K., Heckman, T. M., Weaver, K. A., Hoopes, C. G., & Dahlem, M. 2002, ApJ, 568, 689

Sugai, H., Davies, R. I., & Ward, M. J. 2003, ApJL, 584, L9

Torrey, P., Hopkins, P. F., Faucher-Giguère, C.-A., et al. 2017, MNRAS, 467, 2301

Turner, J. L., Beck, S. C., & Ho, P. T. P. 2000, ApJL, 532, L109

Turner, J. L., & Ho, P. T. P. 1985, ApJL, 299, L77

Turner, J. L., Ho, P. T. P., & Beck, S. C. 1998, AJ, 116, 1212

Ulvestad, J. S., & Antonucci, R. R. J. 1997, ApJ, 488, 621

van der Walt, S., Schonberger, J. L., Nunez-Iglesias, J., et al. 2014, PeerJ, 2, e453

Veilleux, S., Maiolino, R., Bolatto, A. D., & Aalto, S. 2020, A&ARv, 28, 2

Walter, F., Bolatto, A. D., Leroy, A. K., et al. 2017, ApJ, 835, 265

Watson, A. M., Gallagher, J. S. I., Holtzman, J. A., et al. 1996, AJ, 112, 534

Wenger, T. V., Bania, T. M., Balser, D. S., & Anderson, L. D. 2013, ApJ, 764, 34

Westmoquette, M. S., Smith, L. J., & Gallagher, J. S., III 2011, MNRAS, 414, 3719

Wynn-Williams, C. G., Becklin, E. E., Matthews, K., & Neugebauer, G. 1979, MNRAS, 189, 163

Zhao, J.-H., & Wright, M. C. H. 2011, ApJ, 742, 50

Zschaechner, L. K., Bolatto, A. D., Walter, F., et al. 2018, ApJ, 867, 111